Title: Mechanism of RSL3-Induced Ferroptotic Cell Death in HT22 Cells: Contributing Role of Protein Disulfide Isomerase

Running title: Role of PDI in RSL3-Induced Ferroptosis

Authors: Ming-Jie Hou[1], Xuanqi Huang[1] and Bao-Ting Zhu[1,2]

Affiliations: [1]Shenzhen Key Laboratory of Steroid Drug Discovery and Development, School of Medicine, The Chinese University of Hong Kong, Shenzhen, Guangdong, 518172, China, and [2]Shenzhen Bay Laboratory, Shenzhen 518172, China.

Corresponding author information: Bao Ting Zhu, School of Medicine, The Chinese University of Hong Kong, 2001 Longxiang Blvd., Longgang District, Shenzhen, Guangdong 518172, China.

E-MAIL: **BTZhu@CUHK.edu.cn**. PHONE: **+086-755-84273851**.

Abbreviations: PDI, protein disulfide isomerase; nNOS, neuronal nitric oxide synthase; iNOS, inducible nitric oxide synthase; NO, nitric oxide; ROS, reactive oxygen species, TrxR1, thioredoxin reductase 1.

Keywords: Protein disulfide isomerase; Thioredoxin reductase 1; Neuronal nitric oxide synthase; Nitric oxide; Reactive oxygen species; Lipid reactive oxygen species.

Conflict of interest: The authors declare no conflict of interest.

ABSTRACT

Protein disulfide isomerase (PDI) was recently shown to be involved in mediating erastin-induced, glutathione depletion-associated ferroptosis through nitric oxide synthase (NOS) dimerization and nitric oxide (NO) accumulation. In addition, a recent study reported that RSL3, a known ferroptosis inducer and glutathione peroxidase 4 (GPX4) inhibitor, can strongly inhibit thioredoxin reductase 1 (TrxR1). The present study sought to test a hypothesis that RSL3 might, through its inhibition of TrxR1, facilitate PDI activation (*i.e.*, in a catalytically-active, oxidized state), thereby enhancing RSL3-induced ferroptosis through NOS dimerization and NO accumulation. Using the HT22 mouse neuronal cells as an *in-vitro* model, we show that treatment of these cells with RSL3 can strongly increase nitric oxide synthase (NOS) protein levels, and the PDI-mediated NOS activation (through dimerization) is activated by RSL3, resulting in NO accumulation. Mechanistically, we find that PDI is activated in cells treated with RSL3 resulting from its inhibition of TrxR1, and the activated PDI then catalyzes NOS dimerization, which is followed by accumulation of cellular NO, ROS and lipid-ROS, and ultimately ferroptotic cell death. Genetic or pharmacological inhibition of PDI activity partially abrogates RSL3-induced NOS activation and the subsequent accumulation of cellular NO, ROS/lipid-ROS, and ultimately the induction of ferroptosis in HT22 cells. The results of this study show that PDI activation contributes importantly to RSL3-induced ferroptosis in a cell culture model through the PDI→NOS→NO→ROS/lipid-ROS pathway, in addition to its known inhibition of the GPX4 activity.

INTRODUCTION

Ferroptosis is a form of oxidative cell death [1], and is morphologically distinct from apoptosis-associated characteristics such as cellular shrinkage and plasma membrane blistering [1, 2]. Mechanistically, ferroptosis could be selectively induced through cellular glutathione (GSH) depletion [1] and/or through suppression of glutathione peroxidase 4 (GPX4), an enzyme involved in the reduction of lipid peroxides. RSL3 is a prototypical inducer of ferroptosis [3], and over the past few years, it has been widely thought that RSL3 exerts its ferroptosis-inducing activity primarily through suppression of GPX4 function, which would lead to accumulation of cellular lipid reactive oxygen species (lipid-ROS) [4]. However, a recent study has reported that RSL3 could also strongly inhibit the catalytic activity of thioredoxin reductase 1 (TrxR1) [5]. Because TrxR1 use NADPH as a cofactor to reduce the active-site disulfide bond(s) in thioredoxins, when TrxR1 is inhibited by an inhibitor (such as RSL3), the active site of the thioredoxins would stay in the oxidized state (*i.e.*, containing a disulfide bond) [6].

Protein disulfide isomerase (PDI or PDIA1) is the prototype of the PDI family proteins, which belong to the ubiquitous dithiol/disulfide oxidoreductases of the thioredoxin superfamily [7-9]. PDI is primarily localized in the endoplasmic reticulum of mammalian cells, although a small fraction of this protein is also found in the nucleus, cytosol, mitochondria, plasma membrane and extracellular space [10]. PDI is involved in protein processing by catalyzing the formation of intra- and inter-molecular disulfide bridges in proteins [11]. Our recent studies have shown that PDI plays an important role in mediating glutamate- or erastin-induced, GSH depletion-associated oxidative cytotoxicity through PDI-mediated NOS activation (*i.e.*, homodimer formation through a disulfide bond linkage) which is followed by the accumulation of cellular NO and ROS

and lipid-ROS, and ultimately the induction of ferroptotic cell death [12].

In the present study, we sought to examine the role of PDI in mediating RSL3-induced ferroptosis in HT22 neuronal cells and the mechanism of PDI activation. We found that PDI plays an important contributing role in mediating RSL3-induced ferroptotic cell death in these cells through its ability to catalyze NOS dimerization, which is followed by cellular accumulation of NO, ROS and lipid-ROS, and ultimately ferroptotic cell death. Genetic or pharmacological inhibition of PDI's function could abrogate RSL3-induced ferroptosis. The mechanism by which PDI is activated in RSL3-treated cells is caused by TrxR1 inhibition, and this inhibition would leave more PDI proteins in the oxidized state, which is the active form to catalyze the dimerization of NOS (including both nNOS and iNOS) in HT22 cells.

MATERIALS AND METHODS

Reagents

RSL3 (#SML2234) and *S*-nitroso-*N*-acetylpenicillamine (SNAP, #N3398) were purchased from Sigma-Aldrich (St. Louis, MO, USA). CPZ (chlorpromazine, #S5749), Ferrostatin-1 (Fer-1, #S7243), cystamine (#S3695) and 3-(4,5-dimethylthiazol-2-yl)-2,5-diphenyltetrazolium bromide (MTT, #S6821) were purchased from Selleck Chemicals (Houston, TX, USA). Diaminofluorescein-FM diacetate (DAF-FM-DA, #S0019) and diaminofluorescein-2 diacetate (DCF-DA, #S0033) were purchased from Beyotime Biotechnology (Shanghai, China), and C11-BODIPY-581/591 (#D3861) from Thermo Fishers (Waltham, MA, USA). Anti-PDI (#3501), anti-TrxR1 (#6925) and anti-β-actin (#4970) antibodies were purchased from Cell Signaling Technology (Danvers, MA, USA); anti-GPX4 (#ab125066), anti-nNOS (#ab1376) and anti-iNOS (#ab3523) antibodies were from Abcam (Waltham, MA, USA). TrxR1-siRNAs (#sc-36751) and iNOS-siRNAs (#sc-36092) were purchased from Santa Cruz Biotechnology (Dallas, TX, USA). PDI-siRNAs and nNOS-siRNAs (their sequences described earlier [12]) were purchased from Ruibo Biotechnology (Guangdong, China). The MDA (malondialdehyde) Assay Kit (#M496) was purchased from Dojindo Molecular Technologies (Kumamoto, Japan), and the TrxR1 Activity Assay Kit (#BC1155) from Solarbio (Beijing, China).

Cell culture and cell viability assay

HT22 cells were obtained from the Cell Bank of the Chinese Academy of Sciences (Shanghai, China). The HT22 murine hippocampal neuronal cells were cultured in DMEM supplied with 10% (*v/v*) fetal bovine serum and 1% penicillin and streptomycin, and incubated at 37°C under 5% CO_2. Cells were sub-cultured and used for subsequent experiments when they reached about 80% confluence.

The MTT reduction assay was used to determine the change in gross cell viability. The HT22 cells were usually seeded in 96-well plates at a density of 2,000 cells/well 24 h prior to receiving different experimental treatments. To test the effect of a modulating compound, cells were usually jointly treated with RSL3 and the compound for 24 h. Afterwards, MTT at a final concentration of 0.5 mg/mL was added to each well, and incubated for 2.5 h at 37°C under 5% CO_2. After incubation, the MTT-containing medium was removed and 100 μL DMSO was added to each well to dissolve the MTT formazan. Absorbance of the MTT formazan was measured with a UVmax microplate reader (Molecular Device, Palo Alto, CA, USA) at 560 nm.

siRNA transfection

For siRNA transfection, the procedures were described in our earlier study [12]. Briefly, the siRNAs (at a final concentration of 60 nM) for targeted genes (PDI, iNOS, nNOS, and TrxR) were transfected into HT22 cells 24 h after seeding with Lipofectamine RNA iMAX (Invitrogen). Twenty-four h after siRNA transfection, cells were treated with selected drugs, and subsequently processed for cell viability measurement, fluorescence imaging and immunoblot analysis.

Measurement of cellular NO, ROS and lipid-ROS levels

The cellular levels of NO, ROS and lipid-ROS were jointly determined using analytical flow cytometry and fluorescence/confocal microscopy. The HT22 cells were seeded in 24-well plates at a density of 5×10^4 cells/well 24 h before treatment. Afterwards, the cells were treated with RSL3 ± different modulating compounds for 6 h or as indicated. It is of note that the 6-h RSL3 treatment time was selected based on our initial analysis of the time course of NO, ROS and lipid-ROS accumulation. Prior to fluorescent probe staining, cells were washed with HBSS twice. The cellular levels of NO,

ROS and lipid-ROS were detected after addition of respective cell-permeant fluorescent probes (10 μM DAF-FM-DA for NO detection, 10 μM DCFH-DA for ROS detection, and 10 μM BODIPY™-581/591-C11 for lipid-ROS detection), which were dissolved in 200 μL phenol red- and serum-free DMEM. The cells were incubated at 37°C for an additional 30 min, and washed twice with HBSS. The fluorescence images of cellular NO and ROS were taken using a fluorescence microscope (AXIO, Carl Zeiss Corporation, Germany). The fluorescence images of the cellular lipid-ROS were captured using a confocal laser scanning microscope (LSM 900; Carl Zeiss, Oberkochen, Germany) and analyzed with the Zen software (Carl Zeiss). The quantitative fluorescence intensity reflecting the cellular accumulation NO, ROS and lipid-ROS was detected using a flow cytometer (Beckman Coulter, Brea, CA, USA). Three or more experiments were usually conducted to confirm the observations, and the average fluorescence intensity (mean ± S.D.) based on the replicate measurements in one experiment was calculated with the FlowJo software (FlowJo, LLC, Ashland, USA) and selected for presentation.

For measuring intracellular MDA levels, a MDA Assay Kit was used, and all procedures followed manufacturer's instructions.

Measurement of TrxR1 enzyme activity

The TrxR1 enzyme activity was determined using a commercial kit which is based on the measurement of NADPH-dependent reduction of the disulfide bond in the substrate 5,5'-dithiobis-2-nitrobenzoic acid (DTNB). To determine the effect by RSL3 or auranofin on TrxR1's enzyme activity in cultured HT22 cells, the cells were treated with RSL3 (100 nM) or auranofin (1 μM) for 6 h, and then washed with PBS twice, lysed and centrifuged at 9500 *g* for 10 min (4°C) to collect cellular supernatants. Aliquots of the supernatants were properly diluted and then added into the 96-well plate for

determination of TrxR1 enzyme activity according to manufacturer's instructions. The change in absorbance at 412 nm was recorded using a UVmax microplate reader (Molecular Device, Palo Alto, CA, USA). The relative TrxR1 enzyme activity was calculated as a percentage of the vehicle-treated control cells. To determine the direct inhibition of TrxR1's catalytic activity by RSL3 and auranofin in the *in-vitro* enzymatic assay, the untreated HT22 cells were washed with PBS twice, lysed and then centrifuged at 9500 *g* for 10 min (4°C) to prepare cellular supernatants which contain the TrxR1 enzyme. Different concentrations of RSL3 and auranofin were included in the incubation, and the enzyme activity in each treatment group was determined by monitoring the change in absorbance at 412 nm once every 2 min for up to 150 min. Here it should be noted that in this enzyme activity assay, it is assumed that the NADPH-dependent specific catalytic activity of TrxR1 is inhibited by high concentrations of auranofin (its IC_{50} for TrxR1 is approximately 1.1 nM as determined in this study), and the baseline reading at absorbance 412 nm which cannot be inhibited by 1000 nM auranofin is subtracted.

Immunoblot analysis

After treatment with RSL3 for different durations as indicated, the HT22 cells were collected by trypsinization and centrifugation, and then lysed in the RIPA buffer containing 1% protease inhibitor cocktail on ice for 30 min. Protein concentrations were determined using the BCA Assay Kit (ThermoFisher). For total nNOS and iNOS analysis (including both monomeric and dimeric forms of nNOS and iNOS), samples were heated at 95°C for 5 min with a reducing buffer before loaded onto the electrophoresis gel. To analyze the monomeric and dimeric forms of nNOS and iNOS, the samples were prepared with a non-reducing buffer and were not heated, and the

temperature of the gel was maintained below 15°C during electrophoresis. The proteins were separated using 10% SDS-PAGE gel (for total nNOS and iNOS analysis) or 6% SDS-PAGE gel (for monomeric and dimeric nNOS and iNOS analysis), and then transferred to PVDF membranes. The membranes were incubated for 1 h in 5% skim milk at room temperature, and then incubated with the primary antibody overnight. Afterwards, the membranes were washed three times with TBST at room temperature (10 min each time). The membranes were then incubated with the secondary antibody for 1 h at room temperature and washed with TBST three times before visualization. Desired protein bands were visualized using the chemiluminescence imaging system (Tanon 5200, Shanghai, China).

Statistical analysis

All quantitative experiments and data described in this study were repeated at least three times. The data were usually presented as mean ± S.D. of multiple replicate measurements from one selected representative experiment. Statistical analysis was conducted using one-way ANOVA, followed by Dunnett's *post-hoc* tests for multiple comparisons as needed (GraphPad Prism 7, GraphPad Software, La Jolla, CA). Statistical significance was denoted by $P < 0.05$ (* or $^{\#}$) and $P < 0.01$ (** or $^{\#\#}$) for significant and very significant differences, respectively. In most cases, * and ** denote the comparison for statistical significance between the control group (cells treated with vehicle only) and the cells treated with a chemical, whereas $^{\#}$ and $^{\#\#}$ denote the comparison between the cells treated with RSL3 and the cells jointly treated with RSL3 and another compound. For Western blot quantification, one representative data is shown.

RESULTS

Role of cellular NO, ROS and lipid-ROS accumulation in RSL3-induced ferroptotic cell death

Treatment of HT22 cells with RSL3-induced cell death in time- and dose-dependent manners (**Fig. 1A–1C**). Ferrostatin-1 (Fer-1), a commonly-used lipid-ROS scavenger [13, 14], showed a strong protection against RSL3-induced cytotoxicity in these cells (**Fig. 1D**), which confirms earlier observations [15, 16] reporting that RSL3 induces ferroptotic cell death in cultured HT22 cells.

Our recent studies showed that during erastin-induced, GSH depletion-associated ferroptotic cell death in HT22 cells, there was a time-dependent sequential induction of NO and ROS/lipid-ROS accumulation [12]. To probe whether RSL3-induced ferroptosis in HT22 cells is also related to cellular NO and ROS/lipid-ROS accumulation, we determined the time-dependent changes in cellular NO, ROS and lipid-ROS levels following RSL3 treatment (**Fig. 1E–1J**). Based on measurements from fluorescence microscopy and flow cytometry, we found that treatment of HT22 cells with RSL3 elicited a time-dependent increase in cellular NO levels (**Fig. 1E, 1G, Fig. S1A**). Similarly, the cellular levels of ROS and lipid-ROS were also increased in time- and dose-dependent manners in RSL3-treated cells (**Fig. 1E, 1H, Fig. S1B** for ROS; **Fig. 1F, 1I** for lipid-ROS). Malondialdehyde (MDA), one of the end products of lipid peroxidation and often used as an indicator of cellular lipid peroxidation [17], was increased by RSL3 treatment in a time-dependent manner (**Fig. 1J**). Notably, NO accumulation appeared to occur at a very similar time as did ROS/lipid-ROS accumulation.

To determine whether NO accumulation subsequently led to ROS and lipid-ROS accumulation and ultimately ferroptotic cell death, we studied the effect of 2-(4-

carboxyphenyl)-4,4,5,5-tetramethylimidazoline-1-oxyl-3-oxide (cPTIO), a NO scavenger, in RSL3-treated cells [18]. cPTIO effectively suppressed RSL3-induced accumulation of NO (**Fig. 2A**), ROS (**Fig. 2B**) and lipid-ROS (**Fig. 2C**) in HT22 cells. In addition, cPTIO also attenuated RSL3-induced cell death (**Fig. 2D**).

6-Hydroxy-2,5,7,8-tetramethylchroman-2-carboxylic acid (Trolox), which has a strong ROS-scavenging activity plus a weaker NO-scavenging activity [19], partially abrogated RSL3-induced accumulation of NO (**Fig. 2E**) but strongly abrogated the accumulation of ROS (**Fig. 2F**) and lipid-ROS (**Fig. 2G**), and these effects were associated with a very strong protection against RSL3-induced ferroptotic cell death (**Fig. 2H**).

NAC (*N*-acetyl-*L*-cysteine), another commonly-used antioxidant [20], very strongly abrogated RSL3-induced accumulation of cellular NO (**Fig. 2I, 2J**), ROS (**Fig. 2K**) and lipid-ROS (**Fig. 2L**), and these effects were also associated with a strong protection against RSL3-induced cell death (**Fig. 2M**).

Enhancement of RSL3-induced ferroptotic cell death by sodium nitroprusside

Sodium nitroprusside (SNP) is a NO donor and can directly release NO [21]. To provide further support for an upstream role of NO in RSL3-induced ROS/lipid-ROS accumulation and ferroptosis, we sought to determine the effect of SNP on RSL3-induced ROS/lipid-ROS accumulation and ferroptosis induction in HT22 cells. First, treatment of HT22 cells with SNP alone caused a rapid rise in cellular NO levels (**Fig. 3A, 3B, 3C**), which was accompanied by increase in cellular ROS level (**Fig 3A, 3B, 3D**) and lipid-ROS level (**Fig. 3E**). It is of note while NO accumulation peaked within 0.5 h after SNP exposure, the accumulation of ROS and lipid-ROS lagged slightly behind NO increase, reaching the peak at around 1 h after SNP exposure. In addition, treatment of

HT22 cells with SNP alone also elicited a dose-dependent cytotoxicity (**Fig. 3F**).

It is of note that joint treatment of HT22 cells with RSL3 + SNP (200 μM) drastically sensitized HT22 cells to RSL3-induced ferroptotic cell death (**Fig. 3G**). The observed enhancement of RSL3's cytotoxicity by SNP was associated in a parallel manner with a drastically-enhanced accumulation of cellular ROS (**Fig. 3H, 3I**) and lipid-ROS (**Fig. 3J, 3K, 3L**) in cells jointly treated with RSL3 + SNP. Together, these results provide additional support for the hypothesis that RSL3-induced NO accumulation is an important determinant for accumulation of cellular ROS and lipid-ROS, and subsequently ferroptotic cell death.

Role of NOS induction and activation in RSL3-induced ferroptotic cell death

It is known that the generation of cellular NO is mostly catalyzed by the nitric oxide synthase (NOS), which uses *L*-arginine as its primary substrate [22-24]. There are three known subtypes of NOS, namely, nNOS, iNOS and eNOS [22-24]. Our earlier study showed that while nNOS was readily detected in untreated HT22 cells, iNOS was mostly undetectable [25]. In this study, we found that treatment of HT22 cells with increasing concentrations of RSL3 for different durations did not significantly affect total cellular nNOS protein levels (including both monomer and dimer forms) (**Fig. 4A, 4B**). By contrast, while little or no iNOS band was detected in vehicle-treated control HT22 cells as reported earlier [25], treatment of these cells with RSL3 significantly increased the total cellular iNOS levels in a time- and dose-dependent manner (**Fig. 4A, 4B**).

The catalytic activity of NOS is activated through the formation of NOS dimers [22-24], which are stabilized by the intermolecular disulfide bond [26]. Our earlier studies showed that the NOS proteins were activated to form dimers in erastin-treated cells [12,

27]. Next, we sought to determine whether nNOS and iNOS were activated (*i.e.*, dimerized) in RSL3-treated HT22 cells. For nNOS, treatment of HT22 cells with RSL3 significantly increased the formation of nNOS dimers (**Fig. 4B**). For iNOS, RSL3 not only markedly increased the total iNOS protein levels, but also increased iNOS activation (dimerization) in a time- and dose-dependent manner (**Fig. 4B**).

Next, we determined the modulating effect of S-methylisothiourea (SMT) and chlorpromazine (CPZ), two commonly-used NOS inhibitors [28, 29], on RSL3-induced cytotoxicity in HT22 cells. Earlier studies reported that SMT is a preferential inhibitor of iNOS [29, 30], and CPZ is a preferential inhibitor of nNOS [28]. We found that joint treatment of HT22 cells with SMT abrogated RSL3-induced accumulation of cellular NO (**Fig. 4C, 4E**), ROS (**Fig. 4D, 4F**) and lipid-ROS (**Fig. 4G**), and these effects were associated with a strong protection (~100% restoration of cell viability) against RSL3-induced ferroptotic cell death (**Fig. 4H**). In comparison, the effect of CPZ against RSL3-induced accumulation of NO (**Fig. 4C, 4E**), ROS (**Fig. 4D, 4F**) and lipid-ROS (**Fig. 4G**) was relatively weaker, which is also associated with a weaker protection against RSL3-induced cell death (**Fig. 4I**). The combined use of CPZ and SMT at lower concentrations which only produces a partial cytoprotection when each chemical is used alone exerted a stronger protective effect (**Fig. 4J**).

Lastly, we also evaluated in this study the contributing role of nNOS and iNOS in mediating RSL3-induced ferroptotic cell death by using the siRNA approach to selectively knock down their expression in HT22 cells. The efficiency of iNOS and nNOS knockdown was confirmed by measuring changes in cellular nNOS and iNOS protein levels (**Fig. 5A**). Knockdown of iNOS abrogated RSL3-induced increase in iNOS protein levels (**Fig. 5A**), and it also exerted a significant protection against RSL3-induced

cytotoxicity (**Fig. 5B**). By contrast, selective knockdown of nNOS in HT22 cells did not show a significant protective effect (**Fig. 5C**). It is of note that the nNOS knockdown experiment was repeated multiple times, and similar results were obtained which showed a lack of significant protective effect against RSL3-induced cytotoxicity.

Together, these results indicate that NO accumulation resulting from the induction and activation (dimerization) of iNOS and nNOS in RSL3-treated cells is involved in mediating RSL3-induced ferroptosis in HT22 cells. It is apparent that iNOS may play a more dominant role than nNOS in this process.

PDI mediates NOS dimerization in RSL3-treated cells

In this study, we also determined whether PDI could catalyze nNOS and iNOS dimerization in RSL3-treated HT22 cells. The cellular levels of total PDI proteins were not significantly affected by RSL3 treatment (**Fig. 4A**). To provide support for the hypothesis that PDI is responsible for catalyzing nNOS and iNOS dimerization, we determined the effect of cystamine on RSL3-induced ferroptosis. Cystamine is an organic disulfide molecule capable of inhibiting PDI's enzymatic activity through covalent modification of the cysteine residue(s) in its catalytic site [31, 32]. For nNOS, it was observed that treatment of HT22 cells with RSL3 stimulated its activation (dimerization), and joint treatment with cystamine abrogated RSL3-induced nNOS dimerization (**Fig. 5D**). For iNOS, RSL3 not only markedly increased its total protein levels, but also increased its dimer formation (**Fig. 5D**). Joint treatment of these cells with cystamine abolished RSL3-induced increase in total iNOS protein level and its dimerization (**Fig. 5D**). These effects of cystamine on nNOS and iNOS dimerization and on total iNOS protein level in RSL3-treated cells were associated with abrogated

accumulation of NO (**Fig. 5E**), ROS (**Fig. 5F**) and lipid-ROS (**Fig. 5G**), as well as strong protection against RSL3-induced ferroptotic cell death (**Fig. 5H**).

We recently have shown that 4-hydroxyestrone (4-OH-E_1) is an endogenous estrogen metabolite that can effectively inhibit the enzymatic activity of PDI [33]. We found that joint treatment of HT22 cells with 4-OH-E_1 abrogated RSL3-induced increase in total iNOS protein levels (**Fig. 6A**). Because the nNOS dimers are far easier to detect than the iNOS dimers, we thus chose to use the nNOS dimers as a representative parameter to reflect PDI-mediate NOS activation in RSL3-treated HT22 cells. We found that joint treatment of HT22 cells with 4-OH-E_1 abrogated RSL3-induced nNOS dimerization (**Fig. 6A**). This effect was associated with decreased accumulation of cellular NO (**Fig. 6B**), ROS (**Fig. 6C**) and lipid-ROS (**Fig. 6D**), together with increased cell survival (**Fig. 6E**). Similarly, PDI knockdown also elicited a partial protective effect against RSL3-induced cytotoxicity (**Fig. 6F, 6G**).

Our earlier study showed that PDI in untreated HT22 cells is mostly present in the catalytically-inactive *S*-nitrosylated form, and it undergoes *S*-denitrosylation following GSH depletion [25]. To probe the involvement of PDI *S*-denitrosylation in mediating RSL3-induced cytotoxicity in HT22 cells, we studied the effect of *S*-nitroso-*N*-acetylpenicillamine (SNAP), a protein *S*-nitrosylating agent [34]. We found that joint treatment of HT22 cells with SNAP abrogated RSL3-induced NOS activation (based on detection of nNOS dimer; **Fig. 6H**), and this effect was associated with reduced accumulation of NO (**Fig. 6I**), ROS (**Fig. 6J**), lipid-ROS (**Fig. 6K**), and protection against ferroptotic cell death (**Fig. 6L**). These results indicate that *S*-nitrosylation of PDI is indeed associated with suppression of PDI activity, reduction in NOS dimerization, reduction in cellular NO, ROS and lipid-ROS levels, and ultimately, protection from

ferroptosis.

Role of TrxR1 in RSL3-induced ferroptosis

A recent study reported that RSL3 could inhibit the catalytic activity of TrxR1 [5]. Since PDI belongs to the thioredoxin superfamily and a substrate of TrxR1 [35, 36], next we sought to determine the potential role of TrxR1 in RSL3-induced ferroptotic cell death. First, we used the TrxR1-siRNA approach to transiently knock down its expression in HT22 cells. The effectiveness of TrxR1 knockdown was confirmed by Western blot analysis of the change in TrxR1 protein levels (**Fig. 7A**). As shown in **Fig. 7B**, TrxR1 knockdown partially prevented the cytotoxicity of RSL3 and auranofin, a prototypical inhibitor of TrxR1 [5, 37, 38].

We also determined whether the TrxR1 activity in HT22 cells was inhibited by treatment of cells with RSL3 or auranofin. The HT22 cells were first treated with 0.1 μM RSL3 or 1 μM auranofin for 5 h, then the cells were washed and harvested for preparation of cell lysates. Even after all these preparative steps, the TrxR1 activity contained in the cell lysates was still found to be markedly reduced in RSL3- or auranofin-treated cells (**Fig. 7C**); in comparison, the TrxR1 protein levels remained largely unchanged or slightly increased in these cells (**Fig. 7D, 7E, 7F, 7G**). Jointly, these observations suggest that RSL3 and auranofin can bind to TrxR1 very tightly (most likely covalently) to exert a strong and sustained inhibition of the enzyme activity.

Next, we determined the ability of RSL3 and auranofin to directly inhibit the enzymatic activity of TrxR1 in biochemical assays. The whole cell lysates were prepared from untreated HT22 cells, and then the lysates (which contain TrxR1 enzyme) were used to assay the TrxR1 enzyme activity in the presence or absence of RSL3 or

auranofin. We found that the TrxR1 enzyme activity could be very potently inhibited in a concentration-dependent manner by the presence of auranofin, with an apparent IC_{50} of approximately 1.1 nM (**Fig. 7H**). It is of note that the TrxR1 enzyme inhibition by auranofin became stronger but with prolonged incubation time until it reached a plateau (**Fig. 7I**). This pattern of inhibition is consistent with the earlier observation that auranofin can covalently inhibit TrxR1 [39]. Similarly, the TrxR1 enzyme activity was also dose-dependently inhibited by RSL3, with an apparent IC_{50} of approximately 4 μM (**Fig. 7J**), which is in agreement with the results from a recent study when the purified TrxR1 enzyme was used in the *in vitro* assay [5]. It is of note that the overall pattern of TrxR1 inhibition by RSL3 is similar to the inhibition by auranofin, *i.e.*, a stronger inhibition was observed with prolonged reaction time, until it reached a plateau (**Fig. 7K**).

Next, we determined whether auranofin could induce cytotoxicity in HT22 cells. Treatment of HT22 cells with auranofin alone elicited a concentration-dependent cytotoxicity (**Fig. 8A**). The IC_{50} of auranofin's cytotoxicity is 0.8 μM, which is much higher than its IC_{50} for TrxR1 inhibition. In addition, auranofin-induced cell death could not be protected by Fer-1 (**Fig. 8B**) nor the iron chelator DFO (**Fig. 8C**), two commonly-used protective agents for chemically-induced ferroptosis. Similarly, while auranofin (at the 1 μM concentration) elicited accumulation of cellular NO (**Fig. 8D**) and ROS (**Fig. 8E**), it did not elicit a significant accumulation of lipid-ROS (**Fig. 8F**). Together, these observations suggest that the cell death induced by auranofin at high concentrations (much higher than its IC_{50} for TrxR1 inhibition) is not ferroptosis. In addition, the apoptosis inhibitor z-VAD-FMK and necrosis inhibitor Nec-1 also failed to prevent auranofin-induced cell death (**Fig. 8G, 8H**), indicating that auranofin-induced cytotoxicity in HT22 cells is also not typical apoptosis or necrosis.

Based on the above observations, we also investigated the effect of jointly treating HT22 cells with auranofin + BSO, which is a GSH synthase inhibitor [40, 41]. It is expected that BSO would facilitate the induction of GSH depletion-associated ferroptotic cell death when they were jointly treated with auranofin. In this experimental design, BSO was used at a concentration (such as 6 μM) that did not cause significant cytotoxicity when present alone (**Fig. 9A**). We found that joint treatment of HT22 cells with very low concentrations of auranofin + 6 μM BSO caused a concentration-dependent reduction in cell viability (**Fig. 9B**). Interestingly, the GPX4 protein level was also decreased in the cells jointly treated with auranofin + BSO (**Fig. 9C**). Notably, a similar decrease in GPX4 protein levels was observed in cells treated with RSL3 alone (**Fig. 7D**). The cytotoxicity of auranofin + BSO could be partially rescued by Fer-1 (**Fig. 9D**). Cystamine, an inhibitor of PDI which could effectively prevent RSL3-induced ferroptosis (**Fig. 5H**), also exerted a partial protection against the cell death jointly induced by auranofin and BSO (**Fig. 9E**). Similarly, 4-OH-E_1, which could effectively rescue RSL3-induced cell death (**Fig. 6E**), also exerted a partial protection against the cell death jointly induced by auranofin and BSO (**Fig. 9E**). All these observations suggest that when very low concentrations of auranofin (which are close to its IC_{50} for TrxR1 inhibition) were used under conditions where cellular GSH is depleted, the cell death induced by auranofin is largely ferroptosis, and as expected, the cell death could be partially prevented by both ferroptosis inhibitors and PDI inhibitors.

To provide further support for the above observations, we also analyzed changes in cellular NO, ROS and lipid-ROS accumulation and NOS dimerization following treatment of cells with very low concentrations of auranofin + BSO. We found that under these joint treatment conditions, there was a time-dependent accumulation of cellular NO (**Fig. 9F**), ROS (**Fig. 9G**) and lipid-ROS (**Fig. 9H**). In addition, the dimeric nNOS (detected as a

marker for NOS dimerization) was also significantly increased in a time-dependent manner (**Fig. 9C**). Joint treatment of these cells with cystamine partially abrogated the accumulation of NO (**Fig. 9I**), ROS (**Fig. 9J**) and lipid-ROS (**Fig. 9K**) induced by treatment of auranofin + BSO. Similar observations on the abrogation of NO, ROS and lipid-ROS accumulation were also made when the HT22 cells were jointly treated with 4-OH-E_1 ± auranofin and BSO (**Fig. 9I□9K**).

DISCUSSION

RSL3 is a prototypical ferroptosis inducer, and its ferroptosis-inducing ability is thought to be associated with inhibition of GPX4 [4, 42, 43]. However, a recent study showed that in addition to GPX4 inhibition, RSL3 can also inhibit the enzymatic activity of TrxR1, which would shift the pool of thioredoxins to their oxidized forms. PDI is a member of thioredoxin superfamily, and we hypothesize that RSL3 might, through its inhibition of TrxR1's enzymatic activity [5], keep more cellular PDI proteins in the oxidized form, thereby facilitating RSL3-induced ferroptosis through catalyzing nNOS dimerization, followed by cellular ROS and lipid-ROS accumulation, and ultimately ferroptotic cell death (summarized in **Fig. 10**). Considerable amount of experimental evidence is provided in this study that offers support for this hypothesis.

We find that during the development of RSL3-induced ferroptosis in HT22 neuronal cells, NO accumulation likely is an early event which subsequently leads to the formation and accumulation of ROS and lipid-ROS, contributing to the development of ferroptotic cell death. The supporting evidence includes: First, we find that RSL3 can induce the accumulation of both NO and ROS/lipid-ROS in a time- and dose-dependent manner, although there appears to be no clear time differential in their buildup (the reason for this is provided later) (**Fig. 1, S1**). However, the observations made with SNP, which can directly release NO [21], offer support for this suggestion. We show that SNP can quickly lead to accumulation of cellular ROS and lipid-ROS when present alone in HT22 cells, and it also dramatically sensitizes the cells to RSL3-induced accumulation of ROS/lipid-ROS as well as ferroptosis (**Fig. 3**). Here it is of note that our earlier study showed that during erastin-induced ferroptosis, it is clear that NO accumulation occurred slightly earlier than did ROS/lipid-ROS accumulation in HT22 cells [12]. In

addition, when the HT22 cells were jointly treated with erastin + SNP, the NO accumulation occurred much earlier (due to the rapid release of NO from SNP), and in parallel manner, the ROS/lipid-ROS accumulation also occurred much earlier, lagging shortly behind NO accumulation [12]. These experimental observations jointly suggest that during chemically-induced ferroptosis, NO accumulation occurs first, which can then lead to ROS/lipid-ROS accumulation. The second line of evidence comes from the study of NO scavengers and NOS inhibitors. We find in this study that cPTIO, a NO scavenger, can abrogate RSL3-induced NO accumulation, and this effect is accompanied by abrogation of ROS/lipid-ROS accumulation and ferroptotic cell death (**Fig. 2**). In addition, SMT, an iNOS inhibitor, exerts a strong protection against RSL3-induced NO accumulation, accompanied by abrogation of ROS/lipid-ROS accumulation and ferroptotic cell death (**Fig. 4**). Together, these observations suggest that RSL3-induced NO accumulation contributes to the subsequent accumulation of ROS and lipid-ROS, and ultimately the induction of ferroptotic cell death.

Although RSL3-induced NO accumulation leads to cellular ROS/lipid-ROS accumulation in HT22 cells, it should be noted that RSL3-induced buildup of cellular NO and cellular total ROS (which includes lipid-ROS) do not display a distinguishable time differential; in fact, the accumulation of cellular NO and total ROS occurred nearly at the same time (**Fig. 1, S1**). This unexpected experimental observation likely is attributable to the fact that RSL3 can increase both NO and lipid-ROS accumulation at the same time. RSL3 can increase NO biosynthesis through its direct inhibition of TrxR1, which then leads to PDI activation and NOS dimerization; on the other hand, RSL3 can also directly increase cellular lipid-ROS accumulation (independent of cellular NO accumulation) due to its inhibition of GPX4. Therefore, the buildup of cellular lipid-ROS (which is part of the cellular total ROS) in RSL3-treated cells is the result of both GPX4 inhibition (which

likely occurs first) and NO accumulation (which likely occurs at a slightly later time). Because of these reasons, the accumulation of cellular NO and ROS/lipid-ROS occurs rapidly and almost at the same time after exposure to RSL3 (**Fig. 1, S1**).

It is known that the cellular nitric oxide synthase (NOS) plays a pivotal role in catalyzing the formation of NO [12-16]. While NOS lacks catalytic activity in its monomeric form, its dimeric form exhibits the activity for NO synthesis. In this study, we find that RSL3 treatment induces the formation of nNOS and iNOS dimers in a time- and dose-dependent manner in HT22 cells (**Fig. 4**). Joint treatment of cells with CPZ (a nNOS inhibitor) or with SMT (an iNOS inhibitor) have a protective effect against RSL3-induced NO and ROS/lipid-ROS accumulation as well as cytotoxicity (**Fig. 4**).

Here it is of note that the protective effect of SMT is markedly stronger than that of CPZ. In addition, we find that while iNOS knockdown is associated with a partial abrogation of RSL3's cytotoxicity, nNOS knockdown fails to exert a significant protection (**Fig. 5**). Two potential reasons may underlie the inability to observe a significant protective effect with nNOS knockdown: First, it is likely that the relative contribution of cellular nNOS (which is not induced following RSL3 exposure) to the cellular NO pool is markedly smaller than the contribution of cellular iNOS (which is strongly-induced by RSL3). The other reason might be due to the low effectiveness of a sustained nNOS protein knockdown in live HT22 cells. When all the evidence is jointly considered, it appears that iNOS likely plays a more important role than nNOS in mediating RSL3-induced NO accumulation and the subsequent ferroptotic cell death in HT22 cells.

In this study, we demonstrate that PDI is involved in catalyzing NOS dimer formation in RSL3-treated HT22 cells. Our results show that joint treatment of HT22

cells with RSL3 + cystamine strongly reduces RSL3-induced dimerization of both nNOS and iNOS, the accumulation of NO, and ROS/lipid-ROS, and the oxidative cytotoxicity (**Fig. 5**). Furthermore, it is known that *S*-nitrosylation of the cysteine residues in PDI's active site is an important post-translational regulatory mechanism of its function, which would inactivate its enzymatic activity [44, 45]. Our earlier study showed that PDI in untreated HT22 cells was mostly present in the *S*-nitrosylated form, but following glutamate treatment (which induces cellular GSH depletion), PDI underwent *S*-denitrosylation [25]. In agreement with our earlier observations [25], it is found in this study that with joint treatment of HT22 cells with RSL3 + SNAP (an agent capable of *S*-nitrosylating PDI [25]), RSL3-induced NO, ROS and lipid-ROS accumulation is abrogated, and these effects are accompanied with a strong protection against RSL3-indcued ferroptosis (**Fig. 6**). Together, these observations offer support for the notion that PDI is involved in catalyzing NOS dimerization in RSL3-treated HT22 cells, which subsequently leads to accumulation of NO, ROS and lipid-ROS, and ultimately ferroptotic cell death.

Our recent work demonstrated that EN460 (an inhibitor of ERO1) displayed a strong protective effect against erastin-induced ferroptosis in HT22 cells [12]. Erastin induces ferroptosis by depleting cellular GSH through direct inhibition of system Xc^- [1]. However, EN460 at the same concentrations only have a very weak protective effect against RSL3-induced accumulation of cellular NO, ROS/lipid-ROS, and ferroptotic cell death in HT22 cells (**Supplementary Fig. S2**). These observations are in agreement with the fact that RSL3 is an inhibitor of TrxR1, which catalyzes reduction of the disulfide bonds in PDI's active site. On the other hand, ERO1 is an enzyme that catalyzes the formation of disulfide bonds in PDI's active site [46]. When the cellular TrxR1 activity is inhibited by RSL3, the majority of PDI would stay in the oxidized form,

regardless of the oxidizing activity of the cellular ERO1. As such, even when the catalytic activity of ERO1 is inhibited by EN460, a significant fraction of the PDI proteins would still remain in the oxidized form (as a result of TrxR1 inhibition by RSL3), which would mediate the induction of ferroptosis. This is the reason why it would be difficult to see the protective effect of EN460 when TrxR1 is already inhibited by RSL3. This mechanistic explanation is consistent with our experimental observations obtained in this study and those obtained earlier [12, 33].

Based on the findings of this study, it is evident that RSL3-induced ferroptosis involves two important mechanistic components: one is mediated by the activation of PDI (resulting from TrxR1 inhibition by RSL3), and other component is the inhibition of the GPX4-mediated protection against lipid-ROS. Because of the combination of these two effects, a PDI inhibitor which does not have a direct antioxidant activity is expected to be less efficacious in protecting against RSL3-induced ferroptosis compared to a PDI inhibitor which also has a strong antioxidant activity. For instance, 4-OH-E_1, which was recently identified as an effective PDI inhibitor [33], is found to have a strong protective effect against RSL3-induced ferroptotic cell death. The protective effect of 4-OH-E_1 against RSL3-induced cell death is more potent than its protection against erastin-induced cell death in some of the cell lines (unpublished data). This observation suggests that the direct antioxidant activity of 4-OH-E_1 against lipid-ROS also contributes, to some degrees, to its cytoprotective effect. This explanation is plausible since 4-OH-E_1 is a hydrophobic compound, and its antioxidant activity against cellular lipid peroxides would be more readily manifested in RSL3-treated cells. This explanation is also in line with the observation with cystamine, which can inhibit PDI function but does not have any antioxidant property. Cystamine exerts a less efficacious protection against RSL3-induced ferroptosis in HT22 cells compared to 4-OH-E_1 (**Fig.**

5H, 6E); however, both cystamine and 4-OH-E_1 exert a similarly efficacious protection (90–100% protection) against erastin-induced ferroptosis in the same cells (data not shown).

In this study, we find that the TrxR1's enzyme activity can be directly and potently inhibited by auranofin (with an apparent IC_{50} of approximately 1.1 nM), which is slightly lower than the reported IC_{50} (~20 nM) for human TrxR1 [47] (**Fig. 7H**). Notably, it is observed in this study that when the *in vitro* reaction time is prolonged, the reduction in product formation becomes progressively greater, and there is a sustained reduction in product formation (reflecting a sustained TrxR1 inhibition) (**Fig. 7I**). This observation suggests that auranofin inhibits TrxR1's catalytic activity likely resulting from its covalent modification of the enzyme. If auranofin is only a competitive (*i.e.*, noncovalent) inhibitor of TrxR1, then the reduced product formation in the presence of auranofin is expected to gradually diminish with prolonged reaction time, as observed in a recent study with a similar enzyme when a competitive inhibitor was present [33]. Indeed, earlier studies have reported that auranofin can inactivate TrxR1 by forming covalent diselenide bridges with its Sec498 residue [39, 48].

We find that the potency of RSL3 to inhibit TrxR1 *in vitro* is markedly lower than that of auranofin. RSL3's apparent IC_{50} (approximately 4 μM) detected in this study is in line with the results of an earlier study [5] (**Fig. 7J, 7K**). Based on the similar patterns of TrxR1 inhibition by RSL3 and auranofin *in vitro* observed in this study, it is suggested that RSL3 may also inhibit TrxR1 in a covalent manner. The suggestion is partially supported by the observation made in HT22 cells showing a high-potency inhibition of the TrxR1 activity by RSL3 (**Fig. 7C**). It should be noted that the apparent discrepancy between the high-potency RSL3 inhibition in intact cells (**Fig. 7C**) and the low-potency

inhibition of the TrxR1's catalytic activity in an *in vitro* enzymatic assay (**Fig. 7J**) may suggest that RSL3 cannot readily access the catalytic site of TrxR1 in an aqueous reaction system *in vitro*. A similar phenomenon was also observed in an earlier study with the flavonoid-type compounds: while these compounds could strongly activate the cyclooxygenase's catalytic activity in live cells in culture when present at low nM concentrations, they needed to be present at 100□200 μM concentrations in order to exert a similar activation of the pure enzymes in the *in vitro* enzyme assays [49].

Lastly, it is worth noting that there are seven known PDI proteins in the PDI gene family, which include PDIA1 (commonly referred to as PDI) [50], PDIA2 (also called PDIp, a pancreas-specific PDI) [51], PDIA3 [52], PDIA4 [53], PDIA5 [54], PDIA6 [54] and PDILT [55]. Earlier studies have reported that PDI, PDIA3, PDIA4 and PDIA6 are expressed in neuronal cells [56-62] and the expression of PDI and PDIA3 is often dysregulated in disease states of the nervous system [52, 56-58]. While we have demonstrated in the present study that PDI (PDIA1) plays an important role in mediating RSL3-induced ferroptotic cell death in a neuronal cell line, it is not known whether other PDI family proteins share a similar role in mediating chemically-induced ferroptotic cytotoxicity. Since our results show that selective knockdown of PDI expression only provides a partial protection against RSL3-induced cytotoxicity, this possibility cannot be ruled out, and it certainly will be of interest to explore this possibility in the future.

In conclusion, the results of our present study demonstrate that PDI plays a critical role in mediating RSL3-induced ferroptotic cell death in HT22 cells by catalyzing the dimerization of both nNOS and iNOS, followed by cellular accumulation of NO, ROS and lipid-ROS, and ultimately ferroptotic cell death (summarized in **Fig. 10**). The discovery

of an important role of PDI in mediating chemically-induced ferroptosis suggests that PDI might serve as a potential drug target for protection against ferroptosis-related neuronal degeneration.

Data Availability Statement: The authors confirm that the data supporting the findings of this study are available within the article and its supplementary materials.

Funding: This work was supported, in part, by research grants from Shenzhen Peacock Plan (No. KQTD2016053117035204), the National Natural Science Foundation of China (No. 81630096), Shenzhen Key Laboratory of Steroidal Drug Research (No. ZDSYS20190902093417963) and Shenzhen Bay Laboratory (No. SZBL2019062801007).

REFERENCES

1. Dixon, S.J., et al., *Ferroptosis: an iron-dependent form of nonapoptotic cell death.* Cell, 2012. **149**(5): p. 1060-72.
2. Stockwell, B.R., *Ferroptosis turns 10: Emerging mechanisms, physiological functions, and therapeutic applications.* Cell, 2022. **185**(14): p. 2401-2421.
3. Yang, W.S. and B.R. Stockwell, *Synthetic lethal screening identifies compounds activating iron-dependent, nonapoptotic cell death in oncogenic-RAS-harboring cancer cells.* Chem Biol, 2008. **15**(3): p. 234-45.
4. Yang, W.S., et al., *Regulation of ferroptotic cancer cell death by GPX4.* Cell, 2014. **156**(1-2): p. 317-331.
5. Cheff, D.M., et al., *The ferroptosis inducing compounds RSL3 and ML162 are not direct inhibitors of GPX4 but of TXNRD1.* Redox Biol, 2023. **62**: p. 102703.
6. Mustacich, D. and G. Powis, *Thioredoxin reductase.* Biochem J, 2000. **346 Pt 1**(Pt 1): p. 1-8.
7. Tasanen, K., et al., *Characterization of the human gene for a polypeptide that acts both as the beta subunit of prolyl 4-hydroxylase and as protein disulfide isomerase.* J Biol Chem, 1988. **263**(31): p. 16218-24.
8. Pihlajaniemi, T., et al., *Molecular cloning of the beta-subunit of human prolyl 4-hydroxylase. This subunit and protein disulphide isomerase are products of the same gene.* EMBO J, 1987. **6**(3): p. 643-9.
9. Freedman, R.B., T.R. Hirst, and M.F. Tuite, *Protein disulphide isomerase: building bridges in protein folding.* Trends Biochem Sci, 1994. **19**(8): p. 331-6.
10. Turano, C., et al., *Proteins of the PDI family: unpredicted non-ER locations and functions.* J Cell Physiol, 2002. **193**(2): p. 154-63.
11. Cai, H., C.C. Wang, and C.L. Tsou, *Chaperone-like activity of protein disulfide isomerase in the refolding of a protein with no disulfide bonds.* J Biol Chem, 1994. **269**(40): p. 24550-2.
12. Hou, M.J., P. Wang, and B.T. Zhu, *Biochemical mechanism of erastin-induced ferroptotic cell death in neuronal cells.* Acta Biochim Biophys Sin (Shanghai), 2023. **55**(5): p. 853-865.
13. Liu, P., et al., *Ferrostatin-1 alleviates lipopolysaccharide-induced acute lung injury via inhibiting ferroptosis.* Cell Mol Biol Lett, 2020. **25**: p. 10.
14. Miotto, G., et al., *Insight into the mechanism of ferroptosis inhibition by ferrostatin-1.* Redox Biol, 2020. **28**: p. 101328.
15. Peng, W., et al., *L-F001, a Multifunctional Fasudil-Lipoic Acid Dimer Prevents RSL3-Induced Ferroptosis via Maintaining Iron Homeostasis and Inhibiting JNK in HT22 Cells.* Front Cell Neurosci, 2022. **16**: p. 774297.
16. Kato, K., et al., *Quercetin and resveratrol inhibit ferroptosis independently of Nrf2-ARE activation in mouse hippocampal HT22 cells.* Food Chem Toxicol, 2023. **172**: p. 113586.

17. Ayala, A., M.F. Munoz, and S. Arguelles, *Lipid peroxidation: production, metabolism, and signaling mechanisms of malondialdehyde and 4-hydroxy-2-nonenal.* Oxid Med Cell Longev, 2014. **2014**: p. 360438.

18. Maeda, H., et al., *Multiple functions of nitric oxide in pathophysiology and microbiology: analysis by a new nitric oxide scavenger.* J Leukoc Biol, 1994. **56**(5): p. 588-92.

19. Castro, I.A., et al., *Free radical scavenger and antioxidant capacity correlation of alpha-tocopherol and Trolox measured by three in vitro methodologies.* Int J Food Sci Nutr, 2006. **57**(1-2): p. 75-82.

20. Aldini, G., et al., *N-Acetylcysteine as an antioxidant and disulphide breaking agent: the reasons why.* Free Radic Res, 2018. **52**(7): p. 751-762.

21. Zoupa, E. and N. Pitsikas, *The Nitric Oxide (NO) Donor Sodium Nitroprusside (SNP) and Its Potential for the Schizophrenia Therapy: Lights and Shadows.* Molecules, 2021. **26**(11).

22. Andrew, P.J. and B. Mayer, *Enzymatic function of nitric oxide synthases.* Cardiovasc Res, 1999. **43**(3): p. 521-31.

23. Forstermann, U. and W.C. Sessa, *Nitric oxide synthases: regulation and function.* Eur Heart J, 2012. **33**(7): p. 829-37, 837a-837d.

24. Alderton, W.K., C.E. Cooper, and R.G. Knowles, *Nitric oxide synthases: structure, function and inhibition.* Biochem J, 2001. **357**(Pt 3): p. 593-615.

25. Okada, K., M. Fukui, and B.T. Zhu, *Protein disulfide isomerase mediates glutathione depletion-induced cytotoxicity.* Biochem Biophys Res Commun, 2016. **477**(3): p. 495-502.

26. Crane, B.R., et al., *Structure of nitric oxide synthase oxygenase dimer with pterin and substrate.* Science, 1998. **279**(5359): p. 2121-6.

27. Wang, H., P. Wang, and B.T. Zhu, *Mechanism of Erastin-Induced Ferroptosis in MDA-MB-231 Human Breast Cancer Cells: Evidence for a Critical Role of Protein Disulfide Isomerase.* Mol Cell Biol, 2022. **42**(6): p. e0052221.

28. Palacios, M., et al., *Chlorpromazine inhibits both the constitutive nitric oxide synthase and the induction of nitric oxide synthase after LPS challenge.* Biochem Biophys Res Commun, 1993. **196**(1): p. 280-6.

29. Narayanan, K. and O.W. Griffith, *Synthesis of L-thiocitrulline, L-homothiocitrulline, and S-methyl-L-thiocitrulline: a new class of potent nitric oxide synthase inhibitors.* J Med Chem, 1994. **37**(7): p. 885-7.

30. Balaganur, V., et al., *Effect of S-methylisothiourea, an inducible nitric oxide synthase inhibitor, in joint pain and pathology in surgically induced model of osteoarthritis.* Connect Tissue Res, 2014. **55**(5-6): p. 367-77.

31. Fujita, I., et al., *Cystamine-mediated inhibition of protein disulfide isomerase triggers aggregation of misfolded orexin-A in the Golgi apparatus and prevents extracellular secretion of orexin-A.* Biochem Biophys Res Commun, 2017. **489**(2): p. 164-170.

32. Hoffstrom, B.G., et al., *Inhibitors of protein disulfide isomerase suppress apoptosis induced by misfolded proteins.* Nat Chem Biol, 2010. **6**(12): p. 900-6.

33. Wang, H., et al., *Strong Protection by 4-hydroxyestrone against erastin-induced ferroptotic cell death in estrogen receptor-negative human breast cancer cells: evidence for protein disulfide isomerase as a mechanistic target for protection. (submitted).* 2023.

34. Mallis, R.J. and J.A. Thomas, *Effect of S-nitrosothiols on cellular glutathione and reactive protein sulfhydryls.* Arch Biochem Biophys, 2000. **383**(1): p. 60-9.

35. Ali Khan, H. and B. Mutus, *Protein disulfide isomerase a multifunctional protein with multiple physiological roles.* Front Chem, 2014. **2**: p. 70.

36. Lundstrom, J. and A. Holmgren, *Protein disulfide-isomerase is a substrate for thioredoxin reductase and has thioredoxin-like activity.* J Biol Chem, 1990. **265**(16): p. 9114-20.

37. Hwang-Bo, H., et al., *Auranofin, an inhibitor of thioredoxin reductase, induces apoptosis in hepatocellular carcinoma Hep3B cells by generation of reactive oxygen species.* Gen Physiol Biophys, 2017. **36**(2): p. 117-128.

38. Zhang, X., et al., *Repurposing of auranofin: Thioredoxin reductase remains a primary target of the drug.* Biochimie, 2019. **162**: p. 46-54.

39. Becker, K., et al., *Thioredoxin reductase as a pathophysiological factor and drug target.* Eur J Biochem, 2000. **267**(20): p. 6118-25.

40. Drew, R. and J.O. Miners, *The effects of buthionine sulphoximine (BSO) on glutathione depletion and xenobiotic biotransformation.* Biochem Pharmacol, 1984. **33**(19): p. 2989-94.

41. Tagde, A., et al., *The glutathione synthesis inhibitor buthionine sulfoximine synergistically enhanced melphalan activity against preclinical models of multiple myeloma.* Blood Cancer J, 2014. **4**(7): p. e229.

42. Yang, W.S. and B.R. Stockwell, *Ferroptosis: Death by Lipid Peroxidation.* Trends Cell Biol, 2016. **26**(3): p. 165-176.

43. Friedmann Angeli, J.P., et al., *Inactivation of the ferroptosis regulator Gpx4 triggers acute renal failure in mice.* Nat Cell Biol, 2014. **16**(12): p. 1180-91.

44. Uehara, T., et al., *S-nitrosylated protein-disulphide isomerase links protein misfolding to neurodegeneration.* Nature, 2006. **441**(7092): p. 513-7.

45. Kaplan, A., et al., *Small molecule-induced oxidation of protein disulfide isomerase is neuroprotective.* Proc Natl Acad Sci U S A, 2015. **112**(17): p. E2245-52.

46. Araki, K. and K. Nagata, *Functional in vitro analysis of the ERO1 protein and protein-disulfide isomerase pathway.* J Biol Chem, 2011. **286**(37): p. 32705-12.

47. Gromer, S., et al., *Human placenta thioredoxin reductase. Isolation of the selenoenzyme, steady state kinetics, and inhibition by therapeutic gold compounds.* J Biol Chem, 1998. **273**(32): p. 20096-101.

48. Fang, J. and A. Holmgren, *Inhibition of thioredoxin and thioredoxin reductase by 4-hydroxy-2-nonenal in vitro and in vivo.* J Am Chem Soc, 2006. **128**(6): p. 1879-85.

49. Bai, H.W. and B.T. Zhu, *Strong activation of cyclooxygenase I and II catalytic activity by dietary bioflavonoids.* J Lipid Res, 2008. **49**(12): p. 2557-70.

50. Wilkinson, B. and H.F. Gilbert, *Protein disulfide isomerase.* Biochim Biophys Acta, 2004. **1699**(1-2): p. 35-44.

51. Desilva, M.G., et al., *Characterization and chromosomal localization of a new protein disulfide isomerase, PDIp, highly expressed in human pancreas.* DNA Cell Biol, 1996. **15**(1): p. 9-16.

52. Chichiarelli, S., et al., *ERp57/PDIA3: new insight.* Cell Mol Biol Lett, 2022. **27**(1): p. 12.

53. Marcus, N., et al., *Tissue distribution of three members of the murine protein disulfide isomerase (PDI) family.* Biochim Biophys Acta, 1996. **1309**(3): p. 253-60.

54. Ferrari, D.M. and H.D. Soling, *The protein disulphide-isomerase family: unravelling a string of folds.* Biochem J, 1999. **339 (Pt 1)**(Pt 1): p. 1-10.

55. van Lith, M., et al., *PDILT, a divergent testis-specific protein disulfide isomerase with a non-classical SXXC motif that engages in disulfide-dependent interactions in the endoplasmic reticulum.* J Biol Chem, 2005. **280**(2): p. 1376-83.

56. Conway, M.E. and M. Harris, *S-nitrosylation of the thioredoxin-like domains of protein disulfide isomerase and its role in neurodegenerative conditions.* Front Chem, 2015. **3**: p. 27.

57. Andreu, C.I., et al., *Protein disulfide isomerases in neurodegeneration: from disease mechanisms to biomedical applications.* FEBS Lett, 2012. **586**(18): p. 2826-34.

58. Castillo, V., et al., *Functional Role of the Disulfide Isomerase ERp57 in Axonal Regeneration.* PLoS One, 2015. **10**(9): p. e0136620.

59. Di Risola, D., et al., *ERp57 chaperon protein protects neuronal cells from Abeta-induced toxicity.* J Neurochem, 2022. **162**(4): p. 322-336.

60. Paschen, W., et al., *Erp72 expression activated by transient cerebral ischemia or disturbance of neuronal endoplasmic reticulum calcium stores.* Metab Brain Dis, 1998. **13**(1): p. 55-68.

61. Linden, T., J. Doutheil, and W. Paschen, *Role of calcium in the activation of erp72 and heme oxygenase-1 expression on depletion of endoplasmic reticulum calcium stores in rat neuronal cell culture.* Neurosci Lett, 1998. **247**(2-3): p. 103-6.

62. Honjo, Y., et al., *Protein disulfide isomerase-immunopositive inclusions in patients with Alzheimer disease.* Brain Res, 2010. **1349**: p. 90-6.

FIGURE LEGENDS

Figure 1. Time- and dose-dependent accumulation of NO, ROS and lipid-ROS in RSL3-induced ferroptosis in HT22 cells.

A, B. Time- and dose-dependent effect of RSL3 treatment on cell viability (MTT assay, n = 5).

C. Time-dependent change in the gross morphology in RSL3-treated cells (scale bar = 45 μm).

D. Protective effect of Fer-1 against RSL3-induced cytotoxicity following treatment of cells with RSL3 (100 nM) ± Fer-1 (1 μM) for 24 h (MTT assay, n = 5).

E. Time-dependent accumulation of cellular NO and ROS (fluorescence microscopy images, scale bar = 60 μm) following RSL3 treatment, and the quantitative intensity values are shown in the right panel (n = 3).

F. Time-dependent accumulation of cellular lipid-ROS (confocal microscopy images) in RSL3-treated cells (scale bar = 10 μm).

G, H, I. Time-dependent accumulation of cellular NO (**G**), ROS (**H**) and lipid-ROS (**I**) in RSL3-treated cells (analytical flow cytometry). The quantitative intensity values are shown in the right panel (n = 3).

J. Time-dependent change in cellular MDA levels in RSL3-treated cells (n = 3).

Each value represents the mean ± S.D. (* or $^{\#}P < 0.05$; ** or $^{\#\#}P < 0.01$; n.s. not significant).

Figure 2. Effect of free radical scavengers on RSL3-induced cytotoxicity and cellular accumulation of NO, ROS and lipid-ROS in HT22 cells.

A, B, C. Abrogation by cPTIO of RSL3-induced accumulation of cellular NO (**A**), ROS (**B**) and lipid-ROS (**C**). Cells were treated with RSL3 (100 nM) ± cPTIO (200 μM) for 6 h, and then stained for NO, ROS and lipid-ROS (**A, B** for fluorescence microscopy; scale bar = 60 μm; **C** for analytical flow cytometry). The quantitative intensity values are shown in the lower panel (n = 3; the mean value for the control group is labeled next to the bar).

D. Protective effect of cPTIO against RSL3-induced cytotoxicity following treatment of cells with RSL3 (100 nM) ± cPTIO (200 μM) for 24 h (MTT assay, n = 5).

E, F, G. Abrogation by Trolox of RSL3-induced accumulation of cellular NO (**E**), ROS (**F**) and lipid-ROS (**G**). Cells were treated with RSL3 (100 nM) ± Trolox (100 μM) for 6 h, and then stained for NO, ROS and lipid-ROS (**E, F** for fluorescence microscopy; scale bar = 60 μm; **G** for analytical flow cytometry). The quantitative intensity values are shown in the lower panel (n = 3; the mean value for the control group is labeled next to the bar).

H. Protective effect of Trolox against RSL3-induced cytotoxicity following treatment of cells with RSL3 (100 nM) ± Trolox (100 μM) for 24 h (MTT assay, n = 5).

I, J, K, L. Abrogation by NAC of RSL3-induced accumulation of cellular NO (**I, J**), ROS (**K**) and lipid-ROS (**L**). Cells were treated with RSL3 (100 nM) ± NAC (800 μM) for 6 h, and then stained for NO, ROS and lipid-ROS (**J, K** for fluorescence microscopy; scale bar = 60 μm; **I, L** for analytical flow cytometry). The quantitative intensity values are shown in

the lower panel (n = 3; the mean value for the control group is labeled next to the bar).

M. Protective effect of NAC against RSL3-induced cytotoxicity following treatment of cells with RSL3 (100 nM) ± NAC (200, 400 and 800 μM) for 24 h (MTT assay, n = 5).

Each value represents the mean ± S.D. (* or $^{\#}P < 0.05$; ** or $^{\#\#}P < 0.01$; n.s., not significant).

Figure 3. Effect of SNP on RSL3-induced NO, ROS and lipid-ROS accumulation in HT22 cells.

A, B. Levels of NO and ROS after treatment with SNP (200 μM) for different durations (0.5, 1, 2, 4 and 6 h; scale bar = 50 μm) (**A**). The quantitative intensity values are shown in the right panel (n = 3) (**B**).

C, D, E. Time-dependent accumulation of cellular NO (**C**), ROS (**D**) and lipid-ROS (**E**) following SNP treatment (analytical flow cytometry) and the quantitative intensity values are in the right panel (n = 3).

F. Dose-dependent effect of SNP on cell viability (MTT assay, n = 5).

G. Cell viability change following treatment with SNP (200 μM) and different concentrations of RSL3 for 24 h (MTT assay, n = 5).

H, I, J, K, L. Accumulation of ROS (**H, I**) and lipid-ROS (**J, K, L**) after treatment with RSL3 (100 nM) ± SNP (200 μM) (**H** for fluorescence microscopy; scale bar = 60 μm; **J, K, L** for analytical flow cytometry). The quantitative intensity values for **H** are shown in the lower panel (**I**) (n = 3).

Each value represents the mean ± S.D. (* or $^{\#}P < 0.05$; ** or $^{\#\#}P < 0.01$; n.s., not significant).

Figure 4. RSL3-induced NOS activation in HT22 cells.

A. Levels of total iNOS and nNOS proteins following treatment of cells with RSL3 (100 nM) for the indicated time intervals, or with increasing concentrations of RSL3 for 6 h.

B. Levels of the dimer and monomer iNOS and nNOS proteins following treatment of cells with RSL3 (100 nM) for the indicated time intervals, or with increasing concentrations of RSL3 for 6 h.

C, D, E, F, G. Abrogation by SMT and CPZ of RSL3-induced accumulation of cellular NO (**C, E**), ROS (**D, F**) and lipid-ROS (**G**). Cells were treated with RSL3 (100 nM) ± SMT (50 μM) or RSL3 (100 nM) ± CPZ (40 μM) for 6 h, and then stained for NO, ROS and lipid-ROS (**C, D** for fluorescence microscopy; scale bar = 60 μm; **E, F, G** for analytical flow cytometry). The quantitative intensity values are shown on the right panel (n = 3; the mean value for the control group is labeled next to the bar).

H. Protective effect of SMT against RSL3-induced cytotoxicity following treatment of cells with RSL3 (100 nM) ± SMT (25, 50, 100 μM) for 24 h (MTT assay, n = 4).

I. Protective effect of SMT against RSL3-induced cytotoxicity following treatment of cells with RSL3 (100 nM) ± CPZ (40 μM) for 24 h (MTT assay, n = 5).

J. Protective effect of SMT + CPZ against RSL3-induced cytotoxicity following treatment

of cells with RSL3 (100 nM) ± SMT (25 μM) and CPZ (12.5 μM) for 24 h (MTT assay, n = 4).

Each value represents the mean ± S.D. (* or $^{\#}P < 0.05$; ** or $^{\#\#}P < 0.01$; n.s., not significant).

Figure 5. Protective effect of cystamine (a PDI inhibitor) against RSL3-induced ferroptosis in HT22 cells.

A. Effectiveness of iNOS-siRNAs and nNOS-siRNAs in reducing cellular iNOS and nNOS protein levels, respectively. Cells were transfected with iNOS-siRNAs or nNOS-siRNAs for 48 h prior to treatment of cells with RSL3 (50 and 100 nM) for an additional 6 h.

B, C. Effect of iNOS (**B**) and nNOS (**C**) knockdown on RSL3-induced cytotoxicity. Cells were transfected with iNOS-siRNAs or nNOS-siRNAs for 24 h prior to treatment of cells with RSL3 (100 nM) for an additional 24 h.

D. Levels of the dimer and monomer iNOS and nNOS proteins, and the levels of the total iNOS and nNOS proteins after treatment of cells with RSL3 (100 nM) ± cystamine (100 nM) for 6 h.

E, F, G. Abrogation by cystamine of RSL3-induced accumulation of cellular NO (**E**), ROS (**F**) and lipid-ROS (**G**). Cells were treated with RSL3 (100 nM) ± cystamine (100 μM) for 6 h, and then stained for NO, ROS and lipid-ROS (**E, F** for fluorescence microscopy; scale bar = 60 μm; **G** for analytical flow cytometry). The quantitative intensity values are shown in the lower panel (n = 3; the mean value for the control group is labeled next to the bar).

H. Protective effect of cystamine against RSL3-induced cytotoxicity following treatment of cells with RSL3 (100 nM) ± cystamine (100 μM) for 24 h (MTT assay, n = 4).

Each value represents the mean ± S.D. (* or $^{\#}P < 0.05$; ** or $^{\#\#}P < 0.01$; n.s. not significant).

Figure 6. 4-OH-E_1 and SNAP (a *S*-nitrosylating agent) protect against RSL3-induced ferroptosis in HT22 cells.

A. Levels of the dimer and monomer nNOS proteins, and the levels of total iNOS and nNOS proteins after treatment of cells with RSL3 (100 nM) ± 4-OH-E_1 (5 μM) for 6 h.

B, C, D. Abrogation by 4-OH-E_1 of RSL3-induced accumulation of cellular NO (**B**), ROS (**C**) and lipid-ROS (**D**). Cells were treated with RSL3 (100 nM) ± 4-OH-E_1 (5 μM) for 6 h, and then stained for NO, ROS and lipid-ROS (**B, C** for fluorescence microscopy; scale bar = 65 μm; **D** for analytical flow cytometry). The quantitative intensity values are shown in the lower panel (n = 3; the mean value for the control group is labeled next to the bar).

E. Protective effect of 4-OH-E_1 against RSL3-induced cytotoxicity following treatment of cells with RSL3 (100 nM) ± 4-OH-E_1 (1.25, 2.5 and 5 μM) for 24 h (MTT assay, n = 4).

F. Effectiveness of PDI-siRNAs in reducing cellular PDI protein level. Cells were transfected with PDI-siRNAs for 24 and 48 h, respectively, and the PDI protein levels were determined by Western blotting.

G. Protective effect of PDI knockdown on RSL3-induced cytotoxicity. Cells were

transfected with PDI-siRNAs for 24 h prior to treatment of cells with RSL3 (100 nM) for an additional 24 h.

H. Levels of the dimer and monomer nNOS proteins and the total nNOS protein after treatment of cells with RSL3 (100 nM) ± SNAP (200 μM) for 6 h.

I, J, K. Abrogation by SNAP of RSL3-induced accumulation of cellular NO (**I**), ROS (**J**) and lipid-ROS (**K**). Cells were treated with RSL3 (100 nM) ± SNAP (200 μM) for 6 h, and then stained for NO, ROS and lipid-ROS (**I, J** for fluorescence microscopy; scale bar = 65 μm; **K** for analytical flow cytometry). The quantitative intensity values are shown in the right panel (n = 3; the mean value for the control group is labeled next to the bar).

L. Protective effect of SNAP against RSL3-induced cytotoxicity following treatment of cells with RSL3 (100 nM) ± SNAP (200 μM) for 24 h (MTT assay, n = 5).

Each value represents the mean ± S.D. (* or $^{\#}P < 0.05$; ** or $^{\#\#}P < 0.01$; n.s., not significant).

Figure 7. Role of TrxR1 in RSL3-induced ferroptosis in HT22 cells.

A. Effectiveness of TrxR1-siRNAs in reducing cellular TrxR1 protein level. Cells were transfected with TrxR1-siRNAs for 24, 48 and 72 h, and the TrxR1 protein levels were determined by Western blotting.

B. Effect of TrxR1 knockdown on RSL3- and auranofin-induced cytotoxicity. Cells were transfected with TrxR1-siRNAs for 24 h prior to the treatment of RSL3 (100 nM) or auranofin (1 μM) for an additional 24 h, and then cell viability was determined (MTT assay, n = 4).

C. Levels of TrxR1 enzyme activity in cells following treatment with RSL3 (100 nM) or auranofin (1 μM) for 6 h. Cellular supernatants were prepared from different treatment groups (using same numbers of cells), and then the TrxR1 enzyme activity was assayed. The relative TrxR1 activity in the RSL3 and auranofin groups was presented as a percentage of the relative TrxR1 activity in the vehicle-treated control group.

D, E, F, G. Levels of total nNOS, TrxR1 and GPX4 proteins following treatment of cells with RSL3 (100 nM) (**D, F**) or auranofin (1 μM) (**E, G**) for different durations as indicated. The protein bands were determined by densitometry counting (the Image J software). The relative intensity of a given protein was normalized to the corresponding β-actin intensity, and the relative protein level in a given treatment group is presented relative to the vehicle-treated control group.

H, I, J, K. Concentration- and incubation time-dependent inhibition of TrxR1's enzyme activity *in vitro* by auranofin (**H, I**) and RSL3 (**J, K**). The TrxR1 enzyme activity in the presence of an inhibitor (auranofin or RSL3) was presented as % of the control activity in the absence of an inhibitor.

Each value is the mean ± S.D. (* or $^{\#}P < 0.05$; ** or $^{\#\#}P < 0.01$; n.s., not significant).

Figure 8. Effect of auranofin on cell viability and cellular levels of NO, ROS and lipid-ROS in HT22 cells.

A. Dose-dependent effect of auranofin on cell viability (MTT assay, n = 5).

B, C. Effect of Fer-1 (**B**) and DFO (**C**) on auranofin-induced cytotoxicity. The cells were treated with auranofin (1 μM) ± Fer-1 or DFO at indicated concentrations for 24 h, and change in cell viability was determined by MTT assay (n = 5).

D, E, F. Time-dependent accumulation of cellular NO (**D**), ROS (**E**) and lipid-ROS (**F**) in auranofin-treated cells (analytical flow cytometry). The quantitative intensity values are shown in the respective right panels (n = 3).

G. H. Effect of z-VAD-FMK (**G**) and Nec-1 (**H**) on auranofin-induced cytotoxicity. The cells were treated with auranofin (1 μM) ± z-VAD-FMK or Nec-1 at indicated concentrations for 24 h, and change in cell viability was determined by MTT assay (n = 5).

Each value represents the mean ± S.D. (*P < 0.05; **P < 0.01; n.s., not significant).

Figure 9. PDI mediates the cytotoxicity jointly induced by auranofin and BSO in HT22 cells.

A. Dose-dependent effect of BSO on cell viability (MTT assay, n = 4).

B. Dose-dependent effect of auranofin ± BSO on cell viability. The cells were jointly treated with auranofin (25, 50 and 100 nM) ± BSO (2, 4 and 6 μM) for 24 h, and then cell viability was determined by MTT assay (n = 4).

C. Protein levels of the monomer and dimer nNOS, total nNOS, TrxR1 and GPX4 in cells jointly treated with auranofin (50 nM) + BSO (6 μM) for different time intervals as indicated. The relative protein levels are shown in the right panels. The relative intensity of protein bands was normalized to β-actin, and calculated relative to the vehicle (control) group.

D. Protective effect of Fer-1 against cytotoxicity jointly induced by auranofin and BSO. The cells were treated with auranofin (50 nM) + BSO (6 μM) alone or in combination with Fer-1 (1 μM) for 24 h, and cell viability was determined by MTT assay (n = 4).

E. Protective effect of cystamine and 4-OH-E_1 against cell death jointly induced by auranofin + BSO. The cells were treated with auranofin (50 nM) and BSO (6 μM) alone or in combination with cystamine (12.5 μM) or 4-OH-E_1 (2 μM) for 24 h, and cell viability was determined by MTT assay (n = 4).

F, G, H. Time-dependent accumulation of cellular NO (**F**), ROS (**G**) and lipid-ROS (**H**) in cells jointly treated with auranofin and BSO (analytical flow cytometry). The quantitative intensity values are shown in the respective right panels (n = 3).

I, J, K. Abrogation by cystamine and 4-OH-E_1 of auranofin + BSO-induced accumulation of cellular NO (**I**), ROS (**J**) and lipid-ROS (**K**). Cells were treated with auranofin (50 nM) and BSO (6 μM) alone or in combination with cystamine (12.5 μM) or 4-OH-E_1 (2 μM) for 6 h, and then stained for NO, ROS and lipid-ROS (analytical flow cytometry). The quantitative intensity values are shown in the respective right panels (n = 3).

Each value represents the mean ± S.D. (* or $^{\#}P$ < 0.05; ** or $^{\#\#}P$ < 0.01; n.s., not significant).

Figure 10. Schematic illustration of the mechanism by which PDI plays an important contributing role in mediating RSL3-induced ferroptotic cell death in

HT22 cells.

Supplementary Figure S1. **Additional data comparing the time-dependent accumulation of cellular NO (A) and ROS (B) in RSL3-treated cells (analytical flow cytometry)**. All the experimental conditions were the same as described for **Fig. 1G and 1H**, except that a 3-h time point was added in this experiment. Each value is the mean ± S.D. (n = 3).

Each value represents the mean ± S.D. (**$P < 0.01$; n.s., not significant).

Supplementary Figure S2. **Effect of EN460 (a ERO1 inhibitor) on RSL3-induced ferroptosis in HT22 cells**.

A. Effect of EN460 on RSL3-induced cytotoxicity following treatment of cells with RSL3 (100 nM) ± EN460 (5, 10 and 20 μM) for 24 h (MTT assay, n = 4).

B, C, D. Effect of EN460 on RSL3-induced accumulation of cellular NO (**B**), ROS (**C**) and lipid-ROS (**D**). Cells were treated with RSL3 (100 nM) ± EN460 (20 μM) for 6 h, and then stained for NO, ROS and lipid-ROS (**B, C** for fluorescence microscopy; scale bar = 65 μm; **D** for confocal microscopy, scale bar = 10 μm).

Each value represents the mean ± S.D. (* or $^{\#}P < 0.05$; ** or $^{\#\#}P < 0.01$; n.s., not significant).

Figure 1

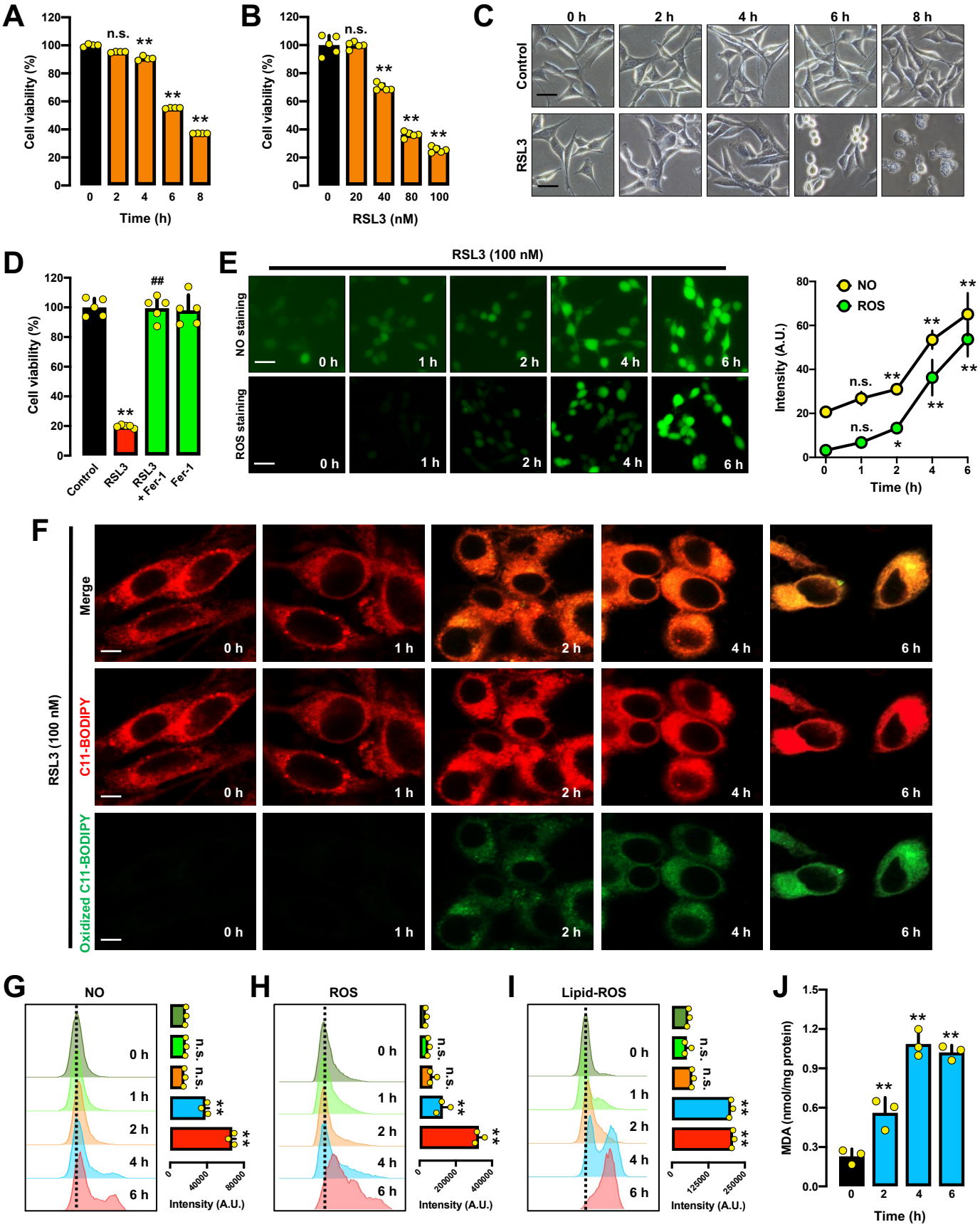
A
Cell viability (%)
Time (h)
n.s.
**
B
Cell viability (%)
RSL3 (nM)
C
0 h
2 h
4 h
6 h
8 h
Control
RSL3
D
Cell viability (%)
##
Control
RSL3
RSL3 + Fer-1
Fer-1
E
RSL3 (100 nM)
NO staining
ROS staining
NO
ROS
Intensity (A.U.)
Time (h)
F
RSL3 (100 nM)
Merge
C11-BODIPY
Oxidized C11-BODIPY
G
NO
H
ROS
I
Lipid-ROS
Intensity (A.U.)
J
MDA (nmol/mg protein)
Time (h)

Figure 2

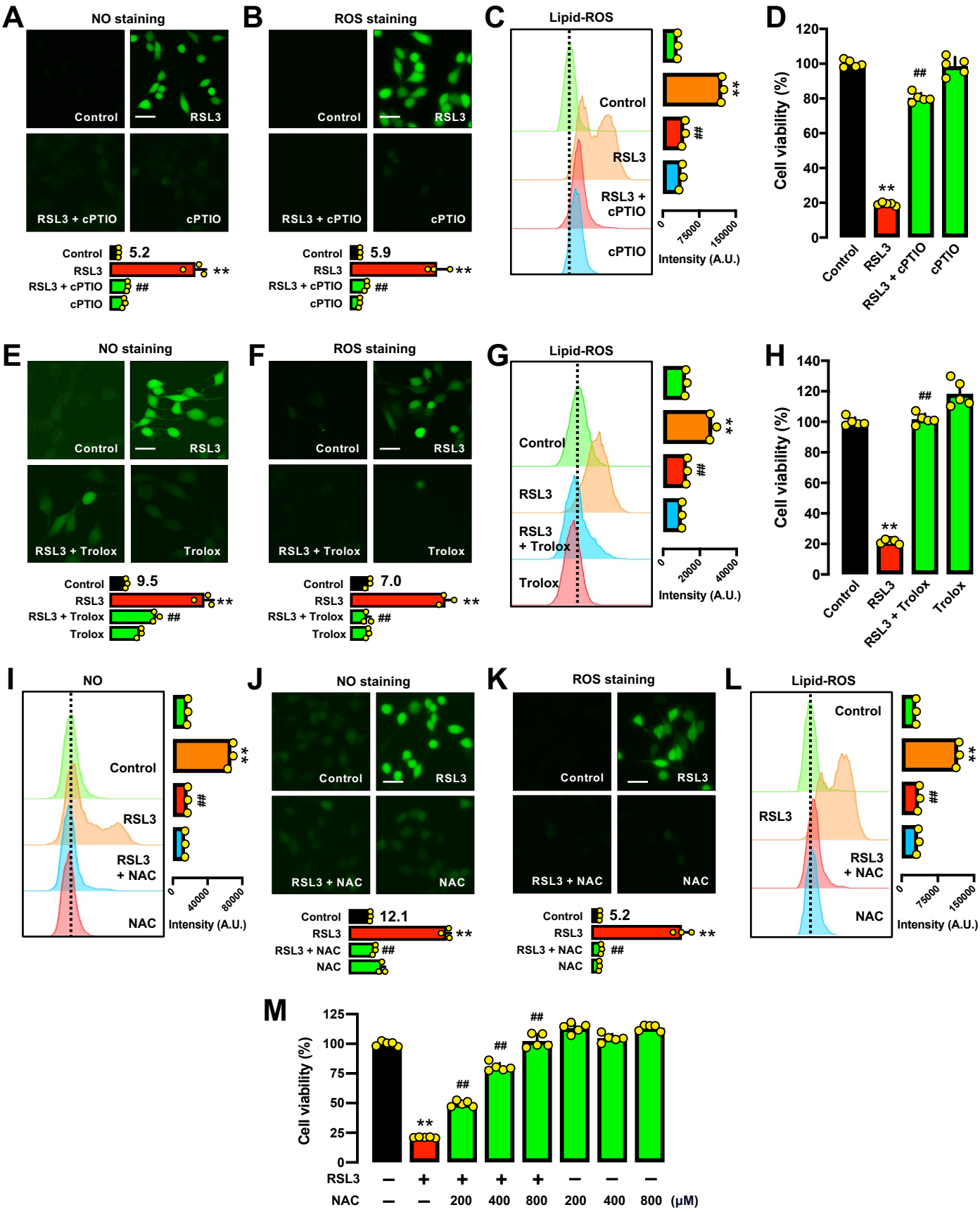
A
NO staining
Control
RSL3
RSL3 + cPTIO
cPTIO
Control 5.2
RSL3 **
RSL3 + cPTIO ##
cPTIO
B
ROS staining
Control
RSL3
RSL3 + cPTIO
cPTIO
Control 5.9
RSL3 **
RSL3 + cPTIO ##
cPTIO
C
Lipid-ROS
Control
RSL3
RSL3 + cPTIO
cPTIO
0 75000 150000
Intensity (A.U.)
D
Cell viability (%)
0 20 40 60 80 100 120
Control RSL3 RSL3 + cPTIO cPTIO
E
NO staining
Control
RSL3
RSL3 + Trolox
Trolox
Control 9.5
RSL3 **
RSL3 + Trolox ##
Trolox
F
ROS staining
Control
RSL3
RSL3 + Trolox
Trolox
Control 7.0
RSL3 **
RSL3 + Trolox ##
Trolox
G
Lipid-ROS
Control
RSL3
RSL3 + Trolox
Trolox
0 20000 40000
Intensity (A.U.)
H
Cell viability (%)
0 20 40 60 80 100 120 140
Control RSL3 RSL3 + Trolox Trolox
I
NO
Control
RSL3
RSL3 + NAC
NAC
0 40000 80000
Intensity (A.U.)
J
NO staining
Control
RSL3
RSL3 + NAC
NAC
Control 12.1
RSL3 **
RSL3 + NAC ##
NAC
K
ROS staining
Control
RSL3
RSL3 + NAC
NAC
Control 5.2
RSL3 **
RSL3 + NAC ##
NAC
L
Lipid-ROS
Control
RSL3
RSL3 + NAC
NAC
0 75000 150000
Intensity (A.U.)
M
Cell viability (%)
0 25 50 75 100 125
RSL3 – + + + + – – –
NAC – – 200 400 800 200 400 800 (μM)

Figure 3

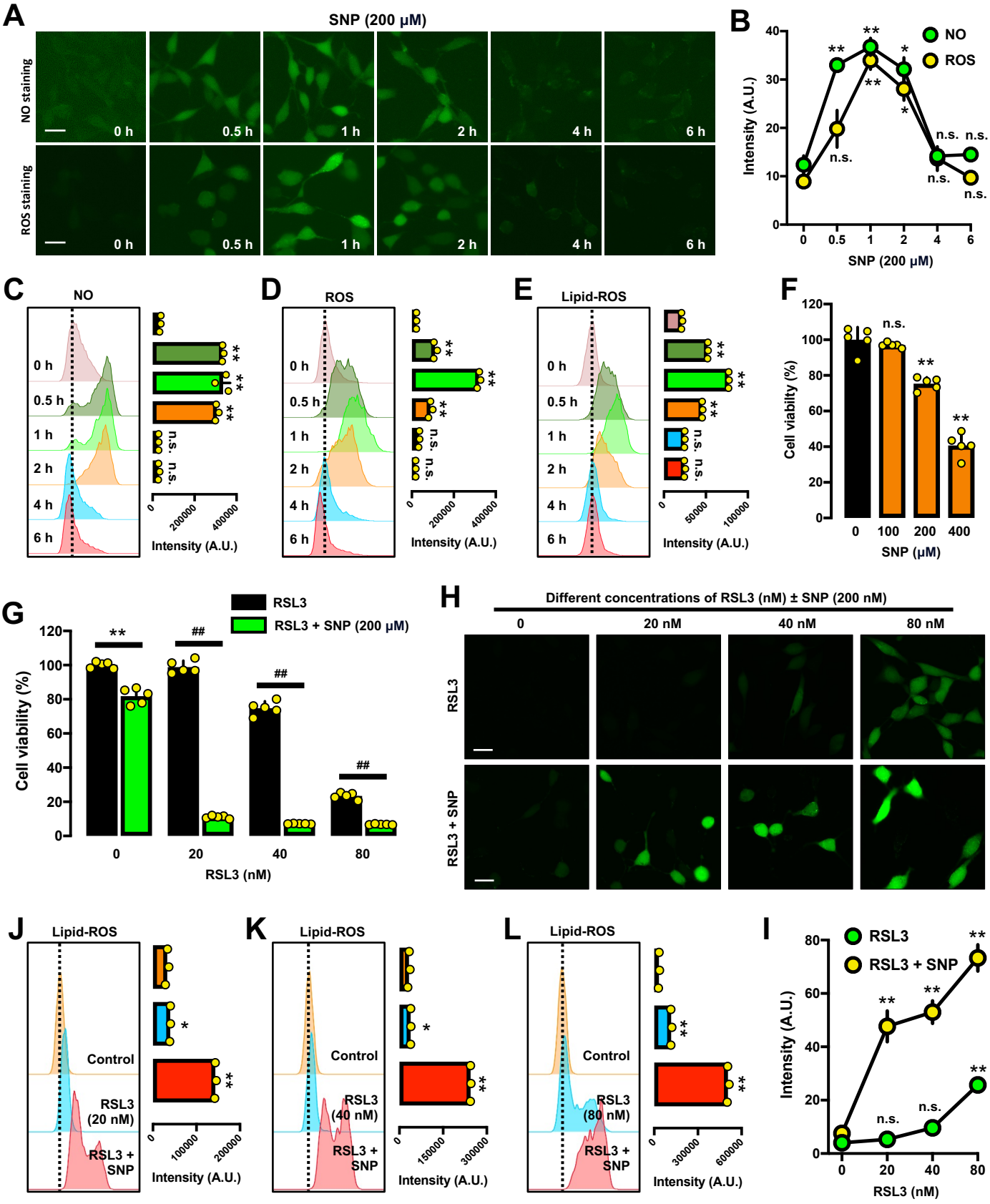
A
SNP (200 μM)
NO staining
ROS staining
0 h
0.5 h
1 h
2 h
4 h
6 h
B
NO
ROS
Intensity (A.U.)
SNP (200 μM)
n.s.
C
NO
D
ROS
E
Lipid-ROS
Intensity (A.U.)
F
Cell viability (%)
SNP (μM)
G
RSL3
RSL3 + SNP (200 μM)
Cell viability (%)
RSL3 (nM)
H
Different concentrations of RSL3 (nM) ± SNP (200 nM)
0
20 nM
40 nM
80 nM
RSL3
RSL3 + SNP
J
Lipid-ROS
Control
RSL3 (20 nM)
RSL3 + SNP
Intensity (A.U.)
K
Lipid-ROS
Control
RSL3 (40 nM)
RSL3 + SNP
Intensity (A.U.)
L
Lipid-ROS
Control
RSL3 (80 nM)
RSL3 + SNP
Intensity (A.U.)
I
RSL3
RSL3 + SNP
Intensity (A.U.)
RSL3 (nM)

Figure 4

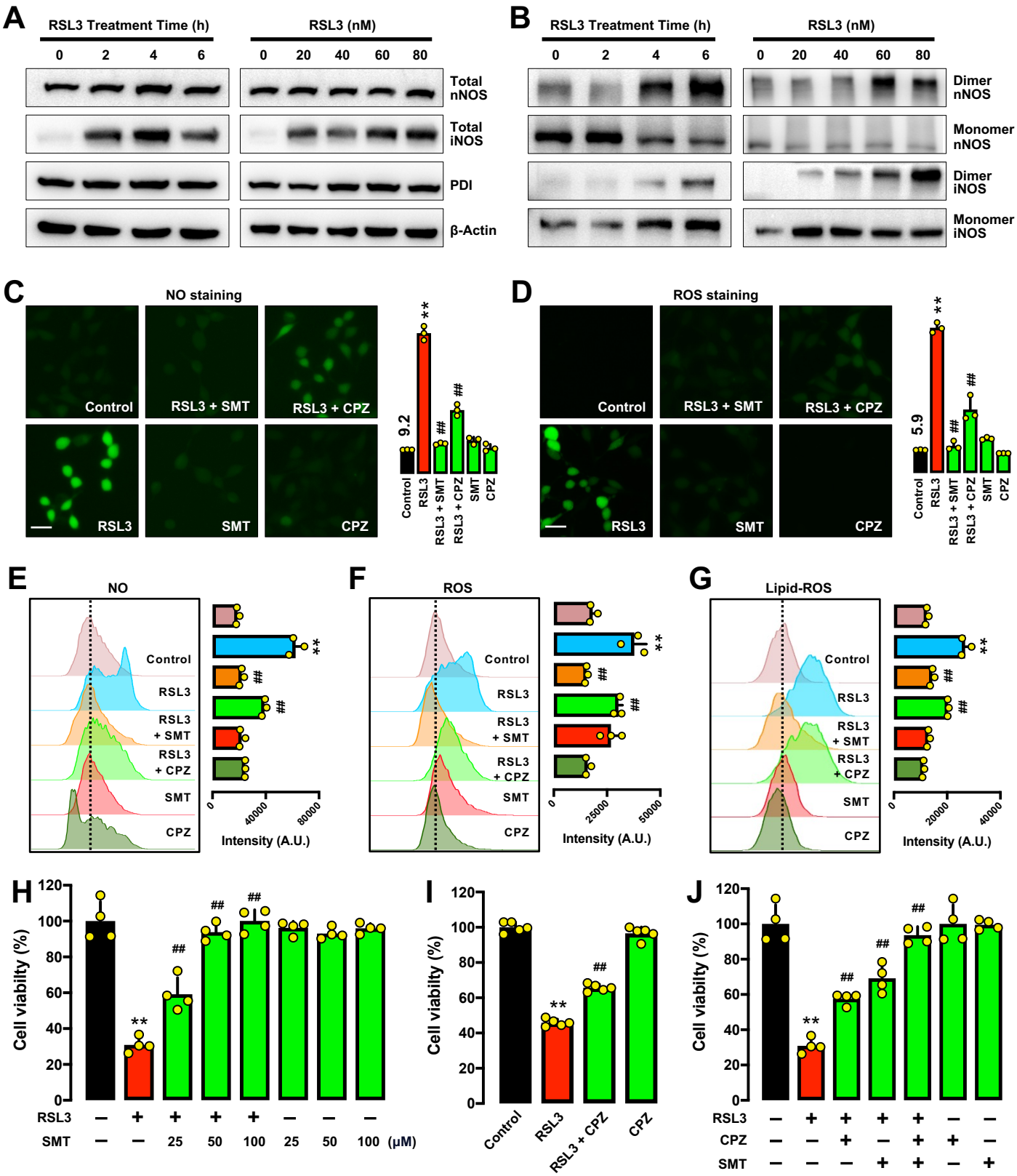
A
RSL3 Treatment Time (h)
0 2 4 6
RSL3 (nM)
0 20 40 60 80
Total nNOS
Total iNOS
PDI
β-Actin
B
RSL3 Treatment Time (h)
0 2 4 6
RSL3 (nM)
0 20 40 60 80
Dimer nNOS
Monomer nNOS
Dimer iNOS
Monomer iNOS
C
NO staining
Control
RSL3 + SMT
RSL3 + CPZ
RSL3
SMT
CPZ
9.2
Control
RSL3
RSL3 + SMT
RSL3 + CPZ
SMT
CPZ
D
ROS staining
Control
RSL3 + SMT
RSL3 + CPZ
RSL3
SMT
CPZ
5.9
Control
RSL3
RSL3 + SMT
RSL3 + CPZ
SMT
CPZ
E
NO
Control
RSL3
RSL3 + SMT
RSL3 + CPZ
SMT
CPZ
0
40000
80000
Intensity (A.U.)
F
ROS
Control
RSL3
RSL3 + SMT
RSL3 + CPZ
SMT
CPZ
0
25000
50000
Intensity (A.U.)
G
Lipid-ROS
Control
RSL3
RSL3 + SMT
RSL3 + CPZ
SMT
CPZ
0
20000
40000
Intensity (A.U.)
H
Cell viability (%)
RSL3
SMT
25
50
100
25
50
100 (μM)
I
Cell viability (%)
Control
RSL3
RSL3 + CPZ
CPZ
J
Cell viability (%)
RSL3
CPZ
SMT

Figure 5

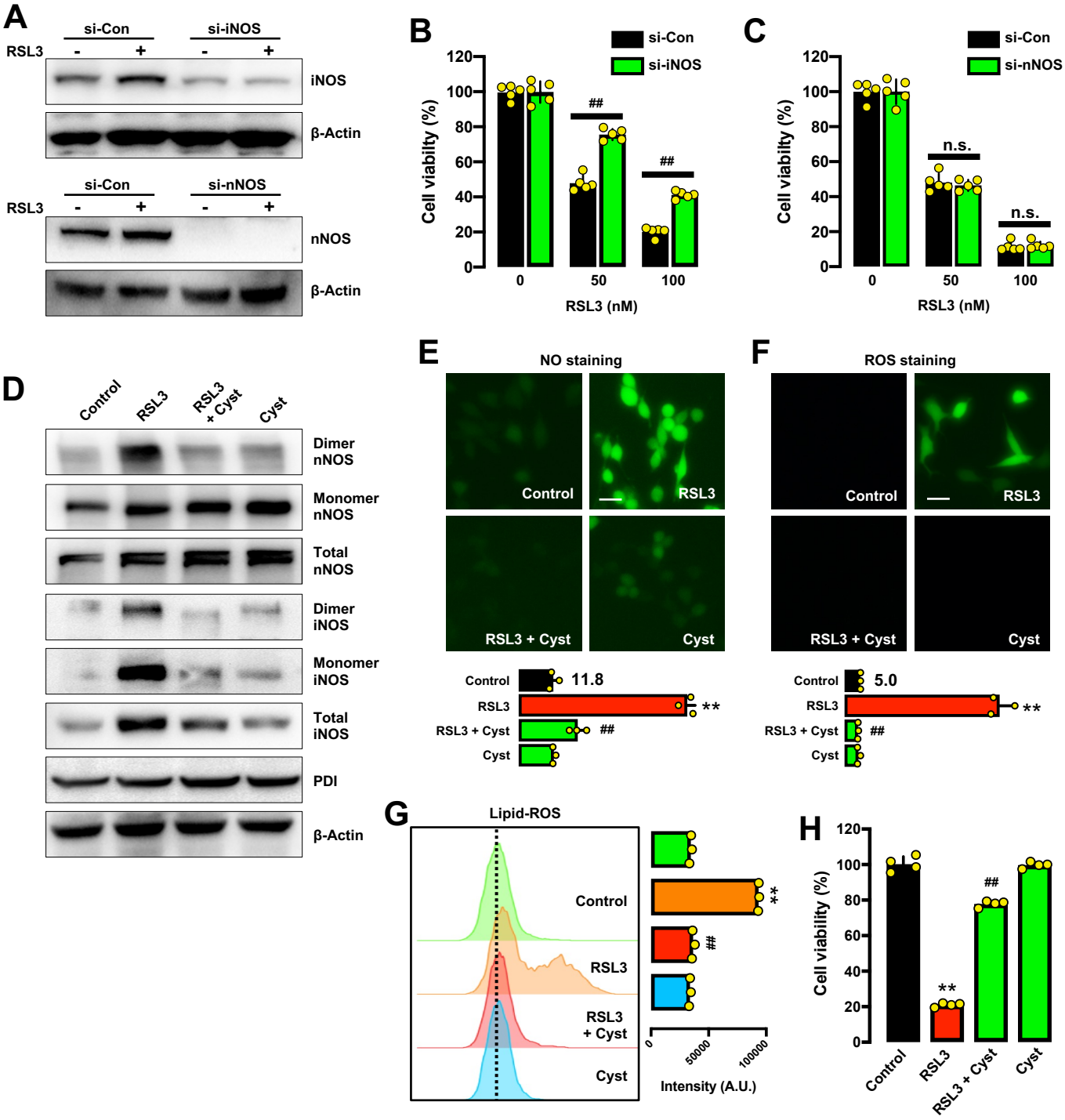
A
si-Con
si-iNOS
RSL3
-
+
-
+
iNOS
β-Actin
si-Con
si-nNOS
RSL3
-
+
-
+
nNOS
β-Actin
B
si-Con
si-iNOS
Cell viability (%)
120
100
80
60
40
20
0
##
##
0
50
100
RSL3 (nM)
C
si-Con
si-nNOS
Cell viability (%)
120
100
80
60
40
20
0
n.s.
n.s.
0
50
100
RSL3 (nM)
D
Control
RSL3
RSL3 + Cyst
Cyst
Dimer nNOS
Monomer nNOS
Total nNOS
Dimer iNOS
Monomer iNOS
Total iNOS
PDI
β-Actin
E
NO staining
Control
RSL3
RSL3 + Cyst
Cyst
Control
11.8
RSL3
**
RSL3 + Cyst
##
Cyst
F
ROS staining
Control
RSL3
RSL3 + Cyst
Cyst
Control
5.0
RSL3
**
RSL3 + Cyst
##
Cyst
G
Lipid-ROS
Control
RSL3
RSL3 + Cyst
Cyst
**
##
0
50000
100000
Intensity (A.U.)
H
Cell viability (%)
120
100
80
60
40
20
0
**
##
Control
RSL3
RSL3 + Cyst
Cyst

Figure 6

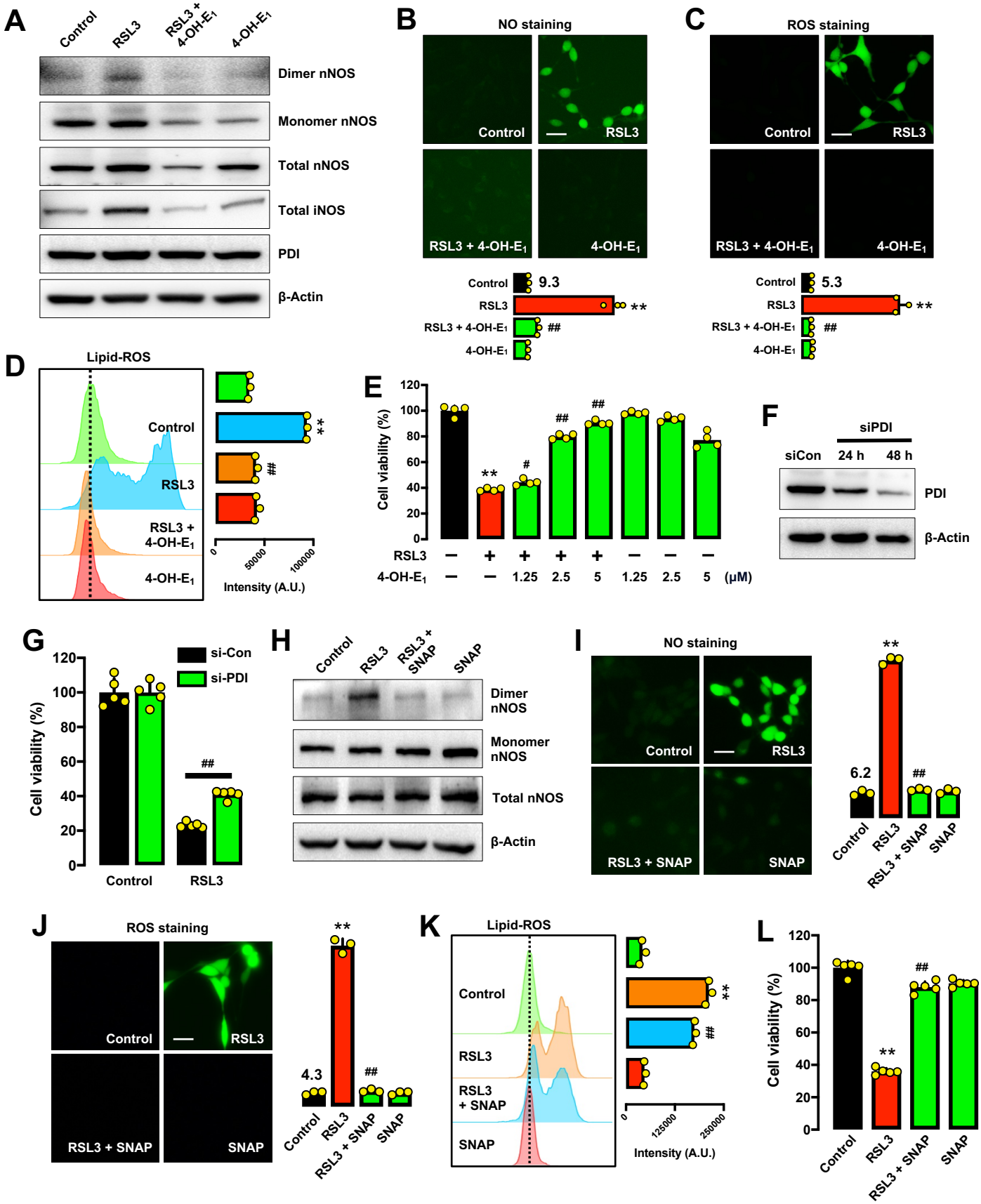
A
Control
RSL3
RSL3 + 4-OH-E1
4-OH-E1
Dimer nNOS
Monomer nNOS
Total nNOS
Total iNOS
PDI
β-Actin
B
NO staining
Control
RSL3
RSL3 + 4-OH-E1
4-OH-E1
9.3
**
##
C
ROS staining
5.3
D
Lipid-ROS
Intensity (A.U.)
E
Cell viability (%)
RSL3
4-OH-E1
(μM)
F
siPDI
siCon
24 h
48 h
G
si-Con
si-PDI
H
RSL3 + SNAP
SNAP
I
6.2
J
4.3
K
L

Figure 7

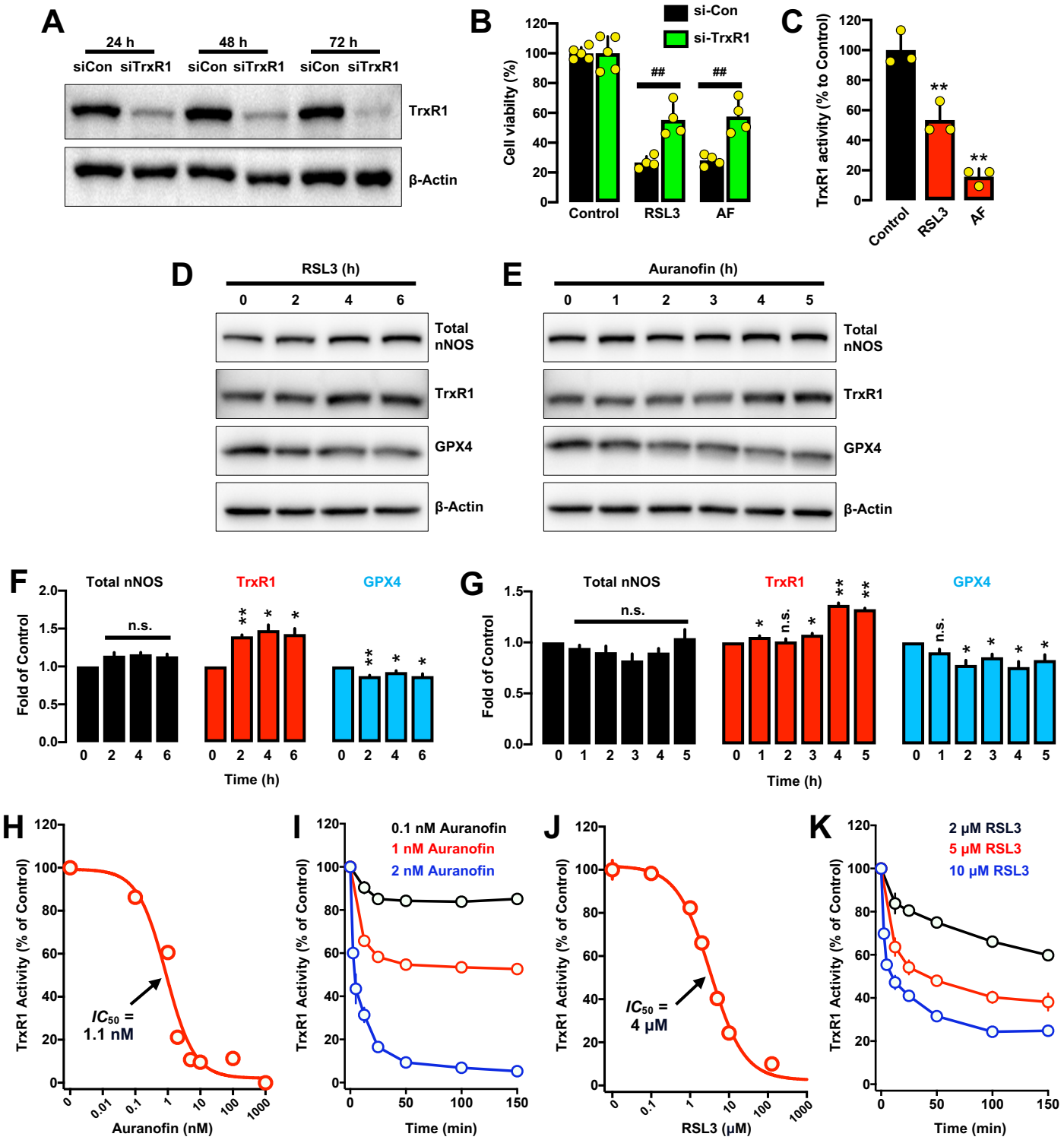
A
24 h
48 h
72 h
siCon siTrxR1 siCon siTrxR1 siCon siTrxR1
TrxR1
β-Actin
B
si-Con
si-TrxR1
Cell viability (%)
##
##
Control
RSL3
AF
C
TrxR1 activity (% to Control)
**
**
Control
RSL3
AF
D
RSL3 (h)
0 2 4 6
Total nNOS
TrxR1
GPX4
β-Actin
E
Auranofin (h)
0 1 2 3 4 5
Total nNOS
TrxR1
GPX4
β-Actin
F
Total nNOS
TrxR1
GPX4
Fold of Control
n.s.
Time (h)
G
Total nNOS
TrxR1
GPX4
Fold of Control
n.s.
Time (h)
H
TrxR1 Activity (% of Control)
IC50 = 1.1 nM
Auranofin (nM)
I
0.1 nM Auranofin
1 nM Auranofin
2 nM Auranofin
TrxR1 Activity (% of Control)
Time (min)
J
TrxR1 Activity (% of Control)
IC50 = 4 μM
RSL3 (μM)
K
2 μM RSL3
5 μM RSL3
10 μM RSL3
TrxR1 Activity (% of Control)
Time (min)

Figure 8

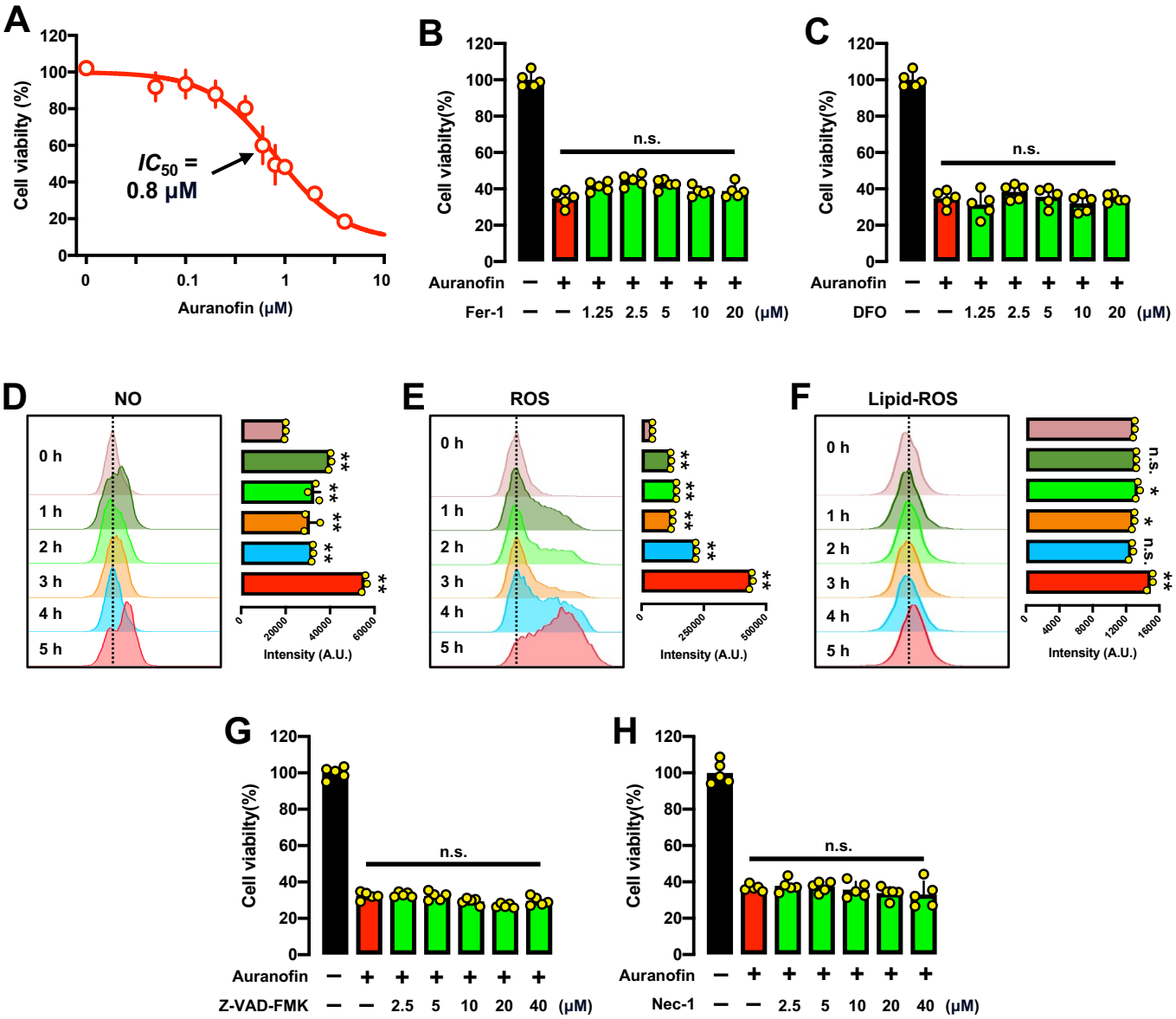
A
Cell viability (%)
IC50 = 0.8 μM
Auranofin (μM)
B
Cell viability(%)
n.s.
Auranofin
Fer-1
1.25 2.5 5 10 20 (μM)
C
Cell viability(%)
n.s.
Auranofin
DFO
1.25 2.5 5 10 20 (μM)
D
NO
0 h
1 h
2 h
3 h
4 h
5 h
Intensity (A.U.)
E
ROS
Intensity (A.U.)
F
Lipid-ROS
Intensity (A.U.)
G
Cell viability(%)
n.s.
Auranofin
Z-VAD-FMK
2.5 5 10 20 40 (μM)
H
Cell viability(%)
n.s.
Auranofin
Nec-1
2.5 5 10 20 40 (μM)

Figure 9

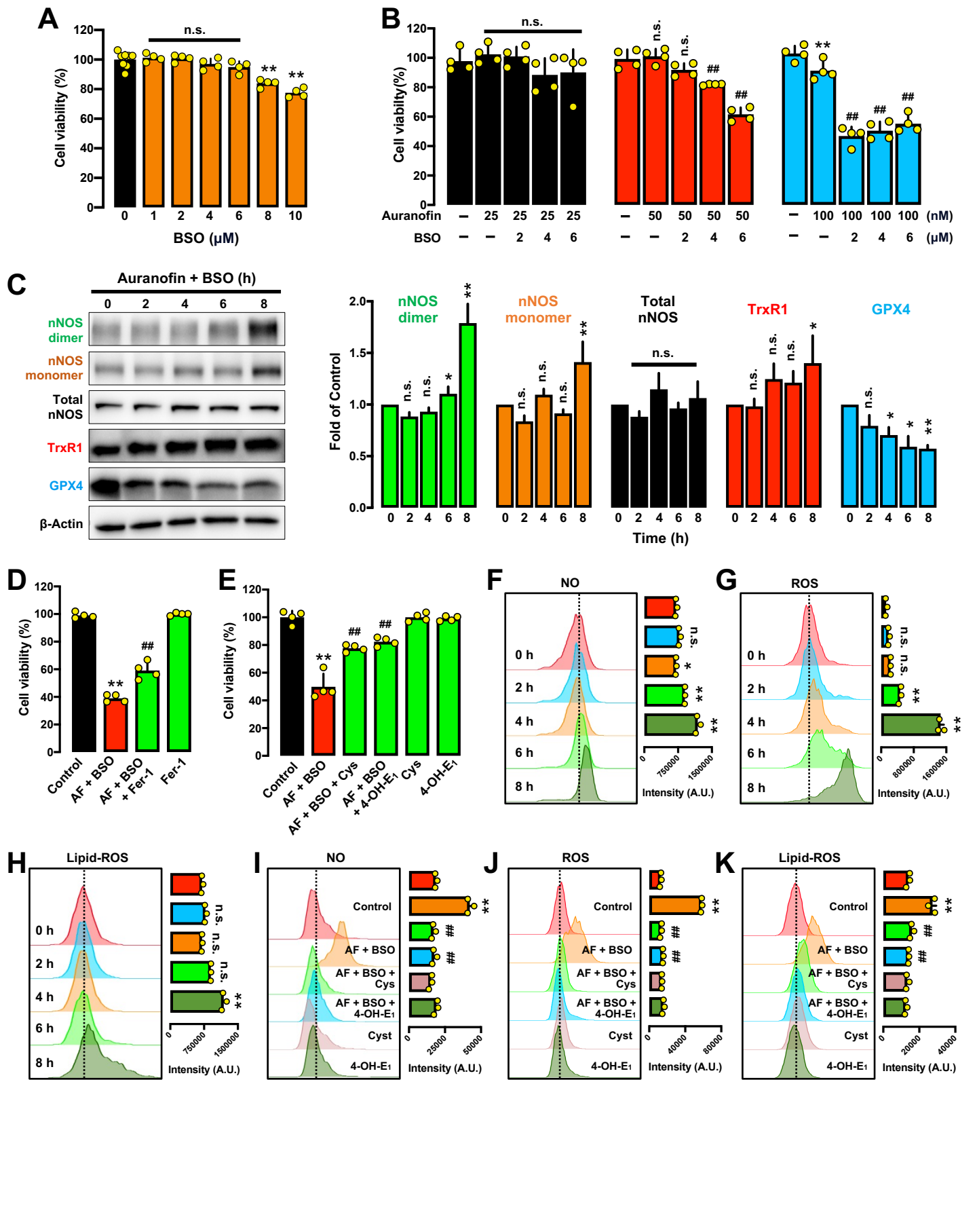
A
Cell viability (%)
n.s.
BSO (μM)
B
Cell viability(%)
Auranofin
BSO
(nM)
(μM)
C
Auranofin + BSO (h)
nNOS dimer
nNOS monomer
Total nNOS
TrxR1
GPX4
β-Actin
Fold of Control
Time (h)
D
Control
AF + BSO
AF + BSO + Fer-1
Fer-1
E
AF + BSO + Cys
AF + BSO + 4-OH-E1
Cys
4-OH-E1
F
NO
G
ROS
H
Lipid-ROS
I
J
K
0 h
2 h
4 h
6 h
8 h
Intensity (A.U.)

Figure 10

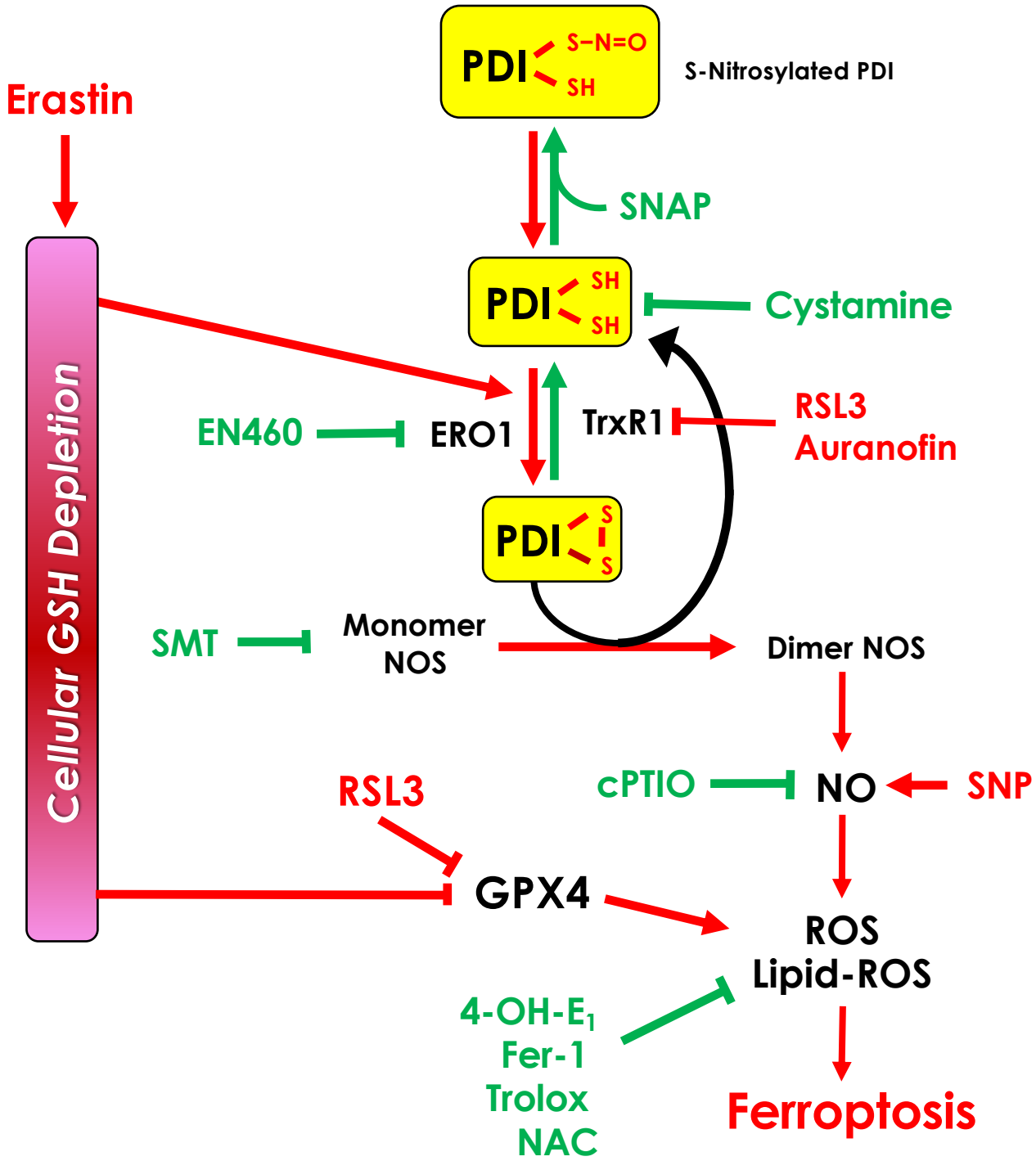
PDI
S–N=O
SH
S-Nitrosylated PDI
Erastin
SNAP
PDI
SH
SH
Cystamine
Cellular GSH Depletion
EN460
ERO1
TrxR1
RSL3
Auranofin
PDI
S
S
SMT
Monomer
NOS
Dimer NOS
RSL3
cPTIO
NO
SNP
GPX4
ROS
Lipid-ROS
4-OH-E1
Fer-1
Trolox
NAC
Ferroptosis